

RESEARCH ARTICLE | JANUARY 06 2025

Leakage characteristics of high performance unplasticized polyvinyl chloride buried pipeline in urban

Zongyuan He (何宗院); Shaowei Hu (胡少伟)  ; Changxi Shan (单常喜); Fuqu Pan (潘福渠)



Physics of Fluids 37, 013314 (2025)

<https://doi.org/10.1063/5.0243910>



Articles You May Be Interested In

Analysis of circular plasmonic photonic crystal fiber for filter applications

AIP Conf. Proc. (March 2020)



Physics of Fluids

Special Topics Open
for Submissions

[Learn More](#)



Leakage characteristics of high performance unplasticized polyvinyl chloride buried pipeline in urban

Cite as: Phys. Fluids **37**, 013314 (2025); doi: 10.1063/5.0243910
 Submitted: 14 October 2024 · Accepted: 11 December 2024 ·
 Published Online: 6 January 2025



View Online



Export Citation



CrossMark

Zongyuan He (何宗院),^{1,2} Shaowei Hu (胡少伟),^{3,a)}  Changxi Shan (单常喜),³ and Fuqu Pan (潘福渠)⁴

AFFILIATIONS

¹College of Civil Engineering and Architecture, Guangxi University, Nanning 530004, China

²Key Laboratory of Disaster Prevention and Structural Safety of Ministry of Education, Guangxi University, Nanning 530004, China

³Yellow River Laboratory, Zhengzhou University, Zhengzhou 450001, China

⁴Shandong Dongxin Plastic Technology Co., Ltd., Bojiqiao St., Yanggu County, Shandong 252300, China

^{a)}Author to whom correspondence should be addressed: hushaowei@zzu.edu.cn

ABSTRACT

The underground pipeline network is an important infrastructure for urban development and also serves as a “lifeline” project for cities. However, due to various factors such as pipeline aging, construction activities, uneven sand settlement, and external loads, underground pipelines often experience leak, leading to water loss. Studying the leakage characteristics can help evaluate the actual degree of leakage loss within the pipeline network. This article considers the influence of three media—sand, water, and air—on the leakage characteristics of pipelines. Initially, leakage simulation experiments were conducted on three different types of leaking pipelines, each exhibiting different leak shapes. Second, the experimental results were compared and analyzed based on existing theoretical models. Subsequently, the Fluent module of ANSYS software was utilized for finite element analysis, ultimately deriving the theoretical formula for the leakage flow rate. The results showed that pipeline leakage led to the formation of an “inverted-cone” sand-water mixing zone and a “semi-elliptical” erosion pit with cracks in sandy media, causing surface oscillations in water media and the formation of water columns spraying outward in air media. The leakage flow rate increases with increasing pressure, and the order of its values under different leakage forms is axial crack > circular hole > circumferential crack. The International Water Association (IWA) model and the fixed and variable area discharges (FAVADs) model can be used to approximate the calculation of the leakage flow rate. Under identical conditions, the leakage flow rate increases on the order of S1, S2, S3, W, and A with changes in the medium and decreases with an increase in burial depth H . The final deformation of each leakage port in the pipeline is approximately elliptical. The value of m increases approximately linearly with the increase in pipeline outer diameter, approximately exponentially with the increase in leakage port size, and approximately exponentially decreases with the increase in pipeline wall thickness and elastic modulus. The FAVAD model is more consistent with finite element results than both the Torricelli (TOR) model and the IWA model. The improved FAVAD model and the S.S.A model provide ideal and reliable calculation results, which can be applied to calculate the leakage flow rate in buried pipelines.

Published under an exclusive license by AIP Publishing. <https://doi.org/10.1063/5.0243910>

I. INTRODUCTION

The buried water supply network is one of the most important pieces of infrastructure in cities, known as the “lifeline project.”¹ Due to factors such as pipeline aging,² engineering construction, uneven sand settlement, and external loads, leaks often occur in the water supply system. This leads to water leakage within the pipeline, which, on the one hand, wastes water resources and causes significant economic losses. On the other hand, under the interaction of water and sand, sand particles are carried away by water, resulting in voids that can easily lead to ground collapse,

seriously threatening people’s lives and property safety, and causing adverse effects on society.^{3–5} Therefore, detecting leaks in buried water supply networks and taking measures to reduce the leakage flow rate is a meaningful topic, and solving this problem requires a deep understanding of the leakage mechanism. Many scholars have conducted extensive research on leakage phenomena and proposed various calculation formulas to describe the leakage flow rate, such as Torricelli (TOR) equation^{6,7}

$$Q = C_d A_0 \sqrt{2gh}. \quad (1)$$

Among them, Q represents the leakage flow rate, measured in m^3/h ; C_d represents the leakage coefficient; A_0 represents the leakage area of the pipeline without pressure, measured in m^2 ; g represents gravitational acceleration, measured in m/s^2 ; h represents the pressure head, measured in m . Since the 1990s, numerous studies have shown that the exponent of h is often higher than that predicted by Eq. (1).^{8,9} Its value is roughly between 0.5 and 2.79. Therefore, based on these findings, the International Water Association (IWA)¹⁰ further developed the formula for calculating the leakage flow rate in exponential form, as shown in

$$Q = c h^\alpha. \quad (2)$$

Here, c represents the leakage coefficient, which depends on A_0 and C_d , and α represents the pressure exponent. May¹¹ believes that α is determined by the material of the pipe and the shape of the leakage port. For pipes with a lower elastic modulus, the leakage area increases with the increase in water head, and the two are linearly related, as shown in

$$A = A_0 + mh. \quad (3)$$

Among them, A represents the leakage area of the pipeline under pressure, measured in m^2 , and m represents the slope of the pressure leakage area line. Many scholars have explored the influence of leakage shape and area on the leakage flow rate through experiments. Ashcroft and Taylor¹² conducted crack leakage tests on polyethylene pipes and found that α ranges from 1.23 to 1.97. Sendil and Dhowalia¹³ conducted on-site testing and found that α is between 0.54 and 1.61, while other related studies^{9,14,15} have shown that α is between 0.5 and 2.5. On this basis, Khadam¹⁶ and Cassa¹⁷ combined the FAVAD theory to divide the leakage flow calculation formula into two parts: constant and variable. They proved that when there is a single leakage, the effect of water pressure on the axial crack area of PVC pipes exhibits a significant linear relationship, and the leakage flow rate is linearly related to the water pressure to the power of 1.5. The relationship between the leakage flow rate and pressure is depicted in

$$Q = ah^{0.5} + bh^{1.5}, \quad a = C_d A_0 \sqrt{2g}, \quad b = C_d m \sqrt{2g}. \quad (4)$$

When there is a complex leakage area, such as axial and transverse intersecting cracks, and the leakage area is linearly related to the square of the water pressure, then the leakage flow rate is linearly related to the 2.5-power of the water pressure,¹⁶ and the leakage flow pressure relationship is expressed in

$$Q = ah^{0.5} + bh^{2.5}. \quad (5)$$

Li *et al.*¹⁸ derived the incremental models for the axial and circumferential crack areas of thin shells using the linear elastic fracture mechanics (LEFM) theory. Subsequently, image analysis techniques were used to measure the leakage area and flow rate, thereby eliminating the influence of the flow coefficient. The derived model was verified through finite element simulation and indoor experiments conducted under various crack sizes and pipeline parameters. Furthermore, the fluid-structure interaction (FSI) simulation was compared with traditional finite element simulations to quantify the impact of leakage hydraulics on the leakage area.

In previous studies on the influence of fluids on buried structures, most have focused on tunnel structures. For example, Wu *et al.*¹⁹

established a numerical model simulating the three-phase flow of water, gas, and sand based on the Euler–Euler method to predict the spatiotemporal flow characteristics inside tunnels after water intrusion. Xie *et al.* systematically studied the dynamic response and failure mechanism caused by water intrusion into the submerged floating tunnel (SFT) pipe, as well as the influence of various factors such as immersion depth, damage opening angle, damage opening area, and external connectivity.²⁰ In addition, there are many studies on the interaction between porous media, such as soil particles, and fluids, as well as the interaction between pipeline structures and fluids,^{21–25} as well as the interaction between pipeline structure and fluid.^{26–28} However, there is little research on the influence of surrounding soil on the leakage characteristics of buried water supply pipelines. Germanopoulos and Jowitt²⁹ studied the impact of different soil particles migrating under hydraulic action on the leakage characteristics of pipelines. Many scholars^{30–34} have analyzed the effects of sand characteristics on pipeline structural behavior and material performance degradation, but they have not conducted further analyses on leakage characteristics. Walski *et al.*³⁵ determined a suitable formula for calculating leakage head losses through experiments. They compared the head losses caused by leakage flow passing through sand and an orifice and introduced a dimensionless constant, OS, to characterize the proportion of these two components. The results indicate that both types of head losses exist during leakage, and when the value of OS is around 1, the proportions of both types of head losses are comparable. When OS is less than 0.01, the head loss of water flowing through the sand accounts for a relatively large proportion, while when OS is greater than 100, the head loss of water flowing through the orifice accounts for a larger proportion. Noack and Ulanicki³⁶ combined the Darcy–Weisbach equation with a two-dimensional sand model to numerically simulate a circular leaking pipeline and studied the influence of sand migration on the pipeline's leakage characteristics. The results showed that the α values of sands with different permeability coefficients ranged between 0.5 and 1. The higher the permeability coefficient, the closer the α value was to 0.5; conversely, the closer it was to 1. Additionally, they also studied the α values for clay and normal sand. After conducting multiple experiments and fitting analyses of the results, they found that the α value for normal sand was 0.3 and for clay was 0.5. Van *et al.*^{37,38} believe that the characteristics of the surrounding sand can affect the leakage characteristics, but the water pressure within the water supply network is independent of the external environment, and changes in the external environment may have a relatively small impact on it. They assumed that the leaking water flow was in the laminar stage and used Darcy's law to quantitatively determine the magnitude of the effect of the surrounding sand on the leakage. However, actual leakage flows are often not laminar, making this research result relatively conservative. Additionally, Van *et al.*³⁹ replaced sand with glass spheres and conducted experiments on fluidization phenomena in the leaking pipeline. The results showed that the size of the leakage port had little effect on the development of the fluidization and moving bed zones. The head loss was small in static sand but large in the flowing bed zone and at the leakage port. Sam *et al.*⁴ analyzed the influence of porous media or geotextile-reinforced porous media surrounding a leaking PE pipeline on its axial crack leakage characteristics. The results showed that the presence of porous media affected the leakage flow rate, reducing it below the inflow rates of air or water. Pike *et al.*⁴⁰ conducted experimental research on the erosion

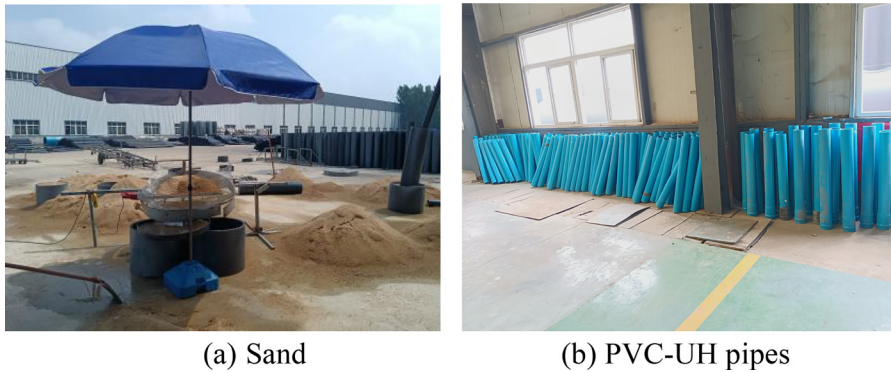


FIG. 1. Experimental materials.

loss caused by the sand fluidization reaction due to water supply pipeline leakage on UPVC pipelines. Through significance analysis, it was shown that the order of significance from low to high in the influencing factors of erosion effect is: burial depth < material < particle size < leakage flow rate < leakage water flow angle. In addition, they found that the smaller the sand particles, the larger the fluidized and moving bed zones, and the slower the erosion of the pipeline by the fluidized mixture. Latifi *et al.*^{41,42} conducted leakage simulation tests on PE pipelines, studied the influence of surrounding sand on leakage characteristics and obtained the correlations between leakage flow rate and various sand parameters. The results indicate that as the sand particle size increases, the leakage flow rate also increases. However, as the sand's viscosity or plasticity increases, the leakage flow rate decreases. The effects of median particle size of sand, permeability coefficient, dry unit weight, and plastic limit are more significant. Additionally, Latifi *et al.*⁴³ also studied the effects of leakage water flow on the sand fluidization and moving bed zones. The results showed that the sizes of the fluidization and moving bed zones varied with water pressure and sand parameters, among which the influence of median particle size was more significant.

In summary, the relationship between leakage flow rate and pressure is generally influenced by leakage hydraulics, pipeline material behavior, sand hydraulics, and other factors. A large amount of research has been conducted on the leakage characteristics of water supply pipelines, including indoor and field experiments, numerical simulations, and theoretical analysis methods. Most studies have focused on the relationship between leakage flow rate and pressure, particularly the determination of the pressure index and leakage coefficient, as well as the factors affecting the leakage flow rate. Research has focused on the influence of leakage area and pipe materials on the leakage flow rate, with the surrounding medium often being air, thereby neglecting the influence of hydraulics on the leakage flow rate. However, the actual leakage phenomena of buried water supply pipelines are often affected by the surrounding medium, and research in this area is relatively rare. At the same time, most previous leakage flow calculation models lack physical significance, and the relevant leakage flow formulas are primarily derived from empirical orifice formulas, lacking stable theoretical support. Building on this, this article focuses on studying the influence of three media—sand, water, and air—on the leakage characteristics of buried pipelines and uses ANSYS Fluent for finite element parameter analysis to derive the theoretical formula of the leakage model. The research results can provide a

reference for subsequent studies and have long-term significance in revealing the leakage mechanisms of water supply pipelines for their maintenance, protection, and management.

II. EXPERIMENTAL PROGRAM

A. Materials

The two main components of the test material are PVC-UH pipe sections and sand, as shown in Fig. 1. PVC-UH pipes are produced by Shandong Dongxin Plastic Technology Co., Ltd., China. The physical and mechanical properties of the pipes meet the relevant requirements of the national standard CJ/T 493–2016,⁴⁴ with an outer diameter (D) of 110 mm and a wall thickness (t) of 4.2 mm. According to the relevant regulations of the standard,⁴⁵ five standard specimens (P1–P5) were extracted from the pipe body and subjected to tensile testing using the UTM-1352 universal testing machine. The measured results are presented in Table I and Fig. 2. The backfill material for plastic water supply pipes is typically medium sand. According to the

TABLE I. Basic physical and mechanical properties of PVC-UH pipes.

Material	ρ (g/cm ³)	E (MPa)	f (MPa)	δ	μ
PVC-UH	1.45	3609	45	85%	0.40

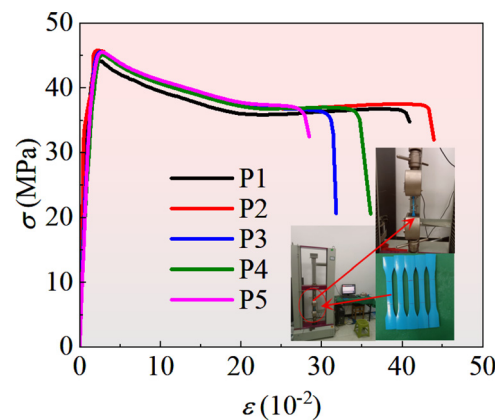


FIG. 2. Stress-strain curves.

09 January 2025 04:38:34

TABLE II. Physical properties of sands.

Sands	Particle size (mm)							C_u	C_c	γ_d (kN/m ³)	K (cm/s)	n
	d_{10}	d_{20}	d_{30}	d_{50}	d_{60}	d_{80}	d_{100}					
S1	0.08	0.15	0.18	0.24	0.30	0.65	5.00	3.75	1.35	17.5	8.10×10^{-3}	0.23
S2	0.19	0.30	0.39	0.55	0.60	0.65	5.00	3.16	1.33	16.3	1.40×10^{-2}	0.25
S3	0.27	0.60	0.80	1.40	1.70	1.90	5.00	6.30	1.39	15.8	3.20×10^{-2}	0.29

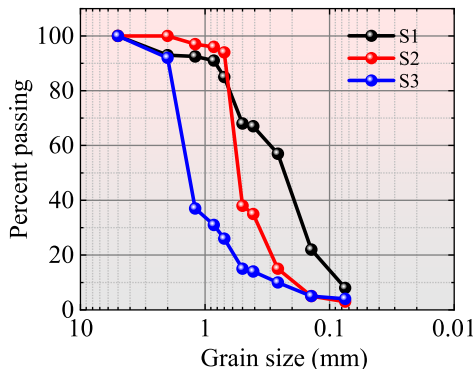


FIG. 3. Grading curves.

specifications,^{46,47} to obtain sand that meets the requirements for buried pipelines, we first screen the sand with a particle size range of 0.075–10 mm before the experiment. During screening, we remove sand with particle sizes greater than 5 mm and less than 0.075 mm. Second, three types of sand samples were prepared from the screened sand, and their physical properties were tested according to the specifications.⁴⁸ The physical properties and grading curves of the sands are presented in Table II and Fig. 3.

B. Experimental pipe sections

The outer diameter of the test pipe section is 110 mm, the wall thickness is 4.2 mm, and the length is 1000 mm. It is connected to the water supply system via a Haval joint. To simulate leakage, three types of leakage openings—circular holes, axial cracks, and circumferential cracks—were prefabricated at the top of the test pipe fittings, as shown in Fig. 4. This experiment considers water leakage in three media—sand, water, and air—along with the burial depth (H) of sand or water. To compare the differences between various types of leaks and eliminate the influence of the initial area, the initial area of each leak was set to 28 mm², and a total of 39 specimens were designed, as shown in

Tables III–V. Among them, DN110 represents a pipe diameter of 110 mm, “O” represents a round hole, “_” represents an axial crack, “|” represents a circumferential crack, S represents sand, W represents water, and A represents air. “1” in S1 represents the first type of sand, and “200” represents a burial depth of 200 mm.

C. Experimental setup

To simulate the leakage conditions of water supply pipelines in sand, water, and air environments, this experiment designed a water supply network system and constructed three iron boxes, which were connected in parallel to the water supply network via openings. The entire water supply network system primarily consists of the following components: water storage tanks, main valves, variable-frequency water pumps (with a head of 160 m), pressure-reducing valves, gate valves, pressure transmitters (0–0.6 MPa), split electromagnetic flow meters (0–160 m³/h), iron boxes, and PVC-UH pipes, as depicted in Fig. 5(a). When assembling the system, insert the water pipe into the iron box through the hole, seal the interface between the hole and the pipe with glue, and ensure there is enough length to overlap with the test pipe section. The on-site diagram of the test setup is presented in Fig. 5(b). The dimensions of the iron box are $L \times W \times H = 2430 \text{ mm} \times 1000 \text{ mm} \times 950 \text{ mm}$, where L , W , and H represent length, width, and height, respectively. The front of the box is not fitted with steel plates, and grooves are positioned along the edges. An organic glass plate of matching size is embedded in the groove and sealed with glue, allowing leakage to be observed through the organic glass during the test. An 18 mm overflow port is located at the bottom of the left side of the iron box and at heights of 200, 300, 400, 500, and 600 mm from the top of the test pipe. The overflow port is located 670 mm from the top of the test pipe and is drained via a rubber hose. This not only allows for the discharge of leaked water but also maintains a constant liquid level height. Leakage situations at various liquid level heights can be assessed. Create a circular hole with a diameter of 120 mm near the glass side at the bottom left corner of the iron box. The center of the hole is 210 mm from the bottom of the sand box and 110 mm from the glass surface. The schematic diagram of the iron box is presented in Fig. 6.

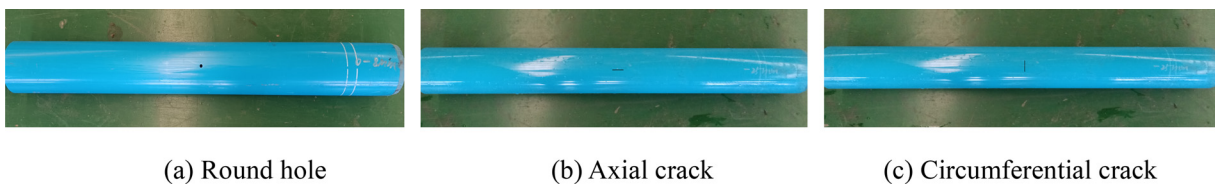


FIG. 4. Design of leakage port in experimental pipe sections.

09 January 2025 04:38:34

TABLE III. Circumferential crack specimens.

Number	Leakage port shape	$l \times w$ (mm)	Medium	H (mm)	A_0 (mm ²)
28S1-200	Circumferential crack	28×1	Sand1	200	28
28S1-400			Sand1	400	
28S1-600			Sand1	600	
28S2-200			Sand2	200	
28S2-400			Sand2	400	
28S2-600			Sand2	600	
28S3-200			Sand3	200	
28S3-400			Sand3	400	
28S3-600			Sand3	600	
28W-200			Water	200	
28W-400			Water	400	
28W-600			Water	600	
28A			Air	200	

D. Experimental procedure and method of measurement

After preparing the testing equipment and the sand required for burying PVC-UH pipes, compact the sand evenly in layers according to the specifications, with each layer being 100 mm thick until the pipe section is buried to a depth of 600 mm. Use a level ruler to level the surface of the sand, with a required compaction degree of 94%.⁴⁷ Adjust the variable-frequency water pump and valves to supply water to the system, with a water pressure range of 10–60 m and an increment of 5 m, which corresponds to the water pressures commonly used in urban water distribution networks. The pressure gauge and flow meter are both connected to the data acquisition system for data collection. The pressure gauge and flow meter are both connected to the data acquisition system for data collection. The average of the pressure gauge readings on both sides is taken as the pressure value for the

TABLE IV. Round hole specimens.

Number	Leakage port shape	d (mm)	Medium	H (mm)	A_0 (mm ²)
○6S1-200	Round hole	6	Sand1	200	28
○6S1-400			Sand1	400	
○6S1-600			Sand1	600	
○6S2-200			Sand2	200	
○6S2-400			Sand2	400	
○6S2-600			Sand2	600	
○6S3-200			Sand3	200	
○6S3-400			Sand3	400	
○6S3-600			Sand3	600	
○6W-200			Water	200	
○6W-400			Water	400	
○6W-600			Water	600	
○6A			Air	200	

TABLE V. Axial crack specimens.

Number	Leakage port shape	$l \times w$ (mm)	Medium	H (mm)	A_0 (mm ²)
-28S1-200	Axial crack	28×1	Sand1	200	28
-28S1-400			Sand1	400	
-28S1-600			Sand1	600	
-28S2-200			Sand2	200	
-28S2-400			Sand2	400	
-28S2-600			Sand2	600	
-28S3-200			Sand3	200	
-28S3-400			Sand3	400	
-28S3-600			Sand3	600	
-28W-200			Water	200	
-28W-400			Water	400	
-28W-600			Water	600	
-8A			Air	200	

test pipe section. The leakage flow rate for the test pipe section under different pressures is determined by the difference in readings between the split electromagnetic flow meters on both sides. Simultaneously, collect the overflow water over a specific period, weigh it, calculate its flow rate, and cross-check it against the value obtained from the electromagnetic flowmeter to verify the accuracy of the test data. Additionally, axial and transverse strain gauges, labeled H1 and Z1, are pasted at the leakage point for reference. Strain gauges labeled H2 and Z2 are also pasted at the midpoint of the distance between the leakage point and the Haval joint, as depicted in Fig. 7, to measure the deformation of the pipe section under pressure. After each pipe test is completed, the water is drained through the overflow port, the sand is excavated, the pipe is replaced, and the test proceeds according to the aforementioned steps.

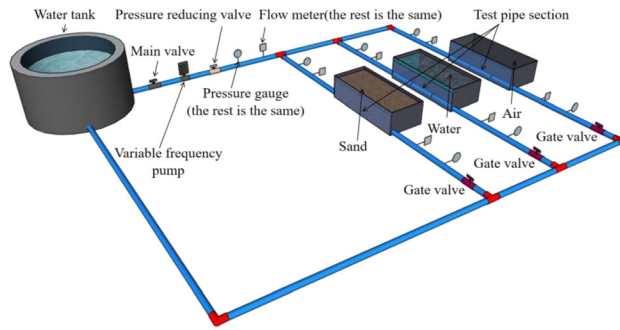
III. TEST RESULTS AND DISCUSSION

A. Experimental phenomena

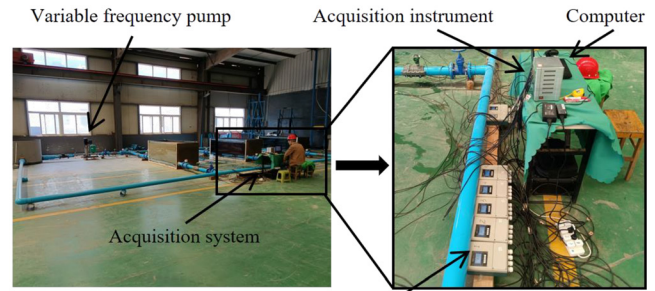
1. Sand box

At the beginning of the experiment, the leaked fluid began to seep into the sand and quickly penetrated in an inverted bowl-shaped manner in all directions. After 5 s, a cavity slowly formed within the sand, and the sand in the cavity area continued to flip and boil. At 10 s, the water in the cavity gathered upward and quickly eroded, causing the surface sand to rise. At 15 s, the water bladder continuously eroded the surrounding sand and continued to spread upward. By 20 s, the water flow broke through the surface of the sand and quickly spread outward to wet the sand. At this time, the water bladder above the pipeline connected to the outside, forming an open fluidized zone. The erosion process intensified, and the upward displacement of the sand ceased. At 60 s of the experiment, the water gathered above the pipeline continuously washed away the surrounding sand, and the water was divided into two areas from top to bottom: the erosion pit area above and the sand-water mixing area below. The upper water body accumulates sand on both sides under the action of erosion force, while the lower water body continues to erode the surrounding sand.

09 January 2025 04:38:34



(a) Schematic diagram



(b) On-site photos

FIG. 5. Experimental setup.

At 180 s, the sand-water mixed zone eventually developed into an inverted cone-shaped erosion zone. The experiment was halted when the disturbance range of the erosion zone remained unchanged. The sand-water mixed zone drained downward and consolidated, eventually forming a semi-elliptical erosion pit accompanied by sand cracks. The experimental phenomena are detailed in Fig. 8.

2. Water box

At the beginning of the experiment, a trace amount of rising bubbles can be observed above the leakage port, indicating that the leaked fluid is discharged under pressure and carries some excess gas. After the gas discharge is completed, the middle of the water body remains essentially stable, with no obvious changes observed. A “seismic source” forms on the surface of the water body directly above the leakage port, radiating in the form of water waves to the surrounding area, and the water surface is observed to oscillate continuously up and down. The experimental phenomena are detailed in Fig. 9.

3. Air box

At the beginning of the experiment, a sudden upward jet of water was sprayed from the leakage port, approximately perpendicular to the pipeline’s axis. Under different pressures, the flow velocity and intensity of the leaking water column vary. When the pressure is low, only the middle of the axial crack exhibits a water column spraying. As the water pressure increases, the water column widens along the crack’s length and thickens along its width, with a slightly larger width in the

middle part. Applying low water pressure to circumferential cracks and circular leaks results in water jets spraying throughout the length of the crack, with the width of the water jet remaining essentially unchanged throughout the crack’s length. Due to the inability to accurately measure the height of the water jet, barriers are placed above the water jet to prevent splashing and protect the instruments and equipment from wetting. The experimental phenomenon is depicted in Fig. 10.

B. Leakage flow rate pressure curves

Based on the experimental data, we plotted the leakage flow rate-pressure ($Q-h$) relationships for the pipe section in each medium under three different leakage forms, as shown in Figs. 11–13. As shown in the figures, the leakage flow rate Q increases with the increase in pressure h . Under the same pressure, when the outflow’s pressure and burial depth are identical, the order of the leakage flow rate Q is: free outflow > submerged outflow > sand outflow. As the pressure increases, the amplification effect becomes more pronounced. This is because the presence of sand or water offers greater resistance to the leakage flow compared to air leakage. This is because the presence of

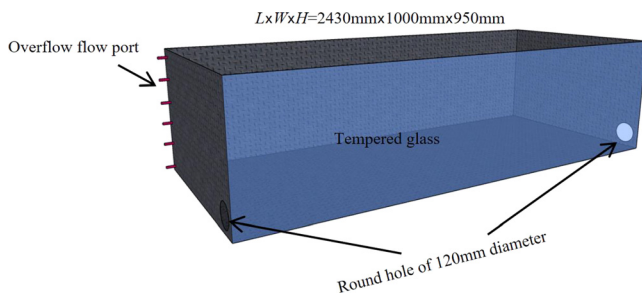


FIG. 6. Schematic diagram of iron box.

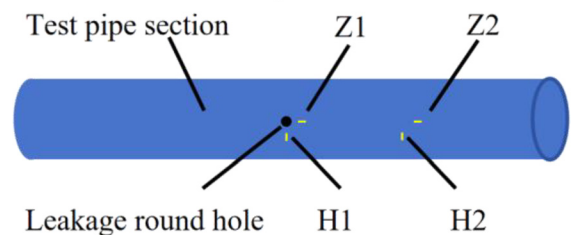


FIG. 7. Layout of strain gauges in the experimental section.

09 January 2025 04:38:34

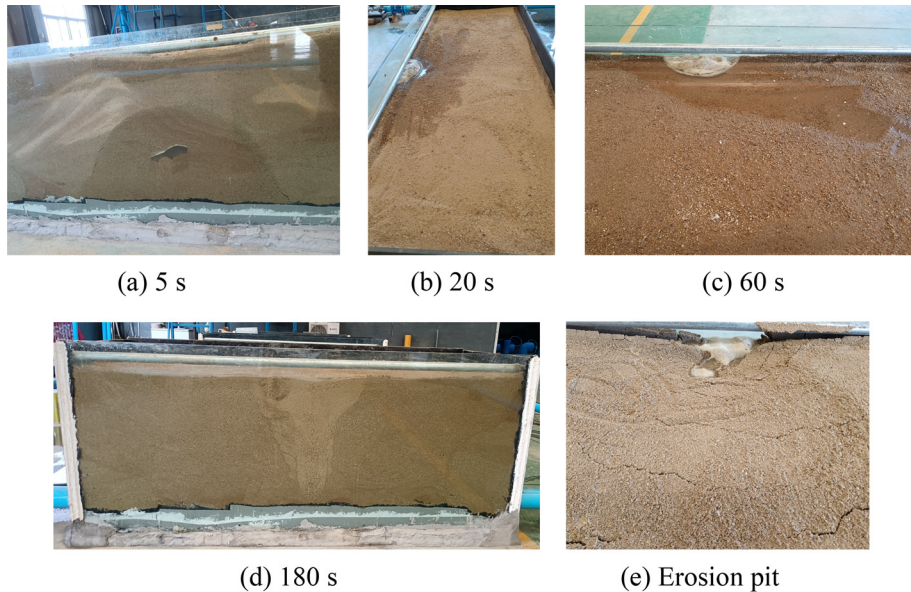


FIG. 8. Phenomenon of sand box.

sand or water creates greater resistance to the leakage flow compared to that in air leakage. The presence of surrounding media materials exerts a reverse hindering effect on the leakage flow, with the hindering effect of sand being more significant than that of water, thereby reducing the leakage flow rate to a certain extent.

Common leakage flow models include the TOR model [Eq. (1)], IWA model [Eq. (2)], and FAVAD model [Eq. (4)]. As shown in Figs. 11–13, the Levenberg–Marquardt optimization algorithm was used to fit and analyze the FAVAD model (black solid line), TOR model (red solid line), and IWA model (blue solid line). The results are presented

in Table VI. From the figures and table, it is evident that for circumferential cracks and circular holes, the traditional TOR model fitting results are not consistent with the experimental results, and the differences are quite significant. The goodness-of-fit R^2 value ranges from 0.7149 to 0.8962, and only the experimental results for axial cracks can be approximated. The R^2 value ranges from 0.9544 to 0.9699, indicating that this model has certain limitations. Overall, the fitting results of the FAVAD model and the IWA model are in good agreement with the experimental results, with a goodness-of-fit R^2 value ranging from 0.9910 to 0.9991. Among them, the index α value of the IWA model's

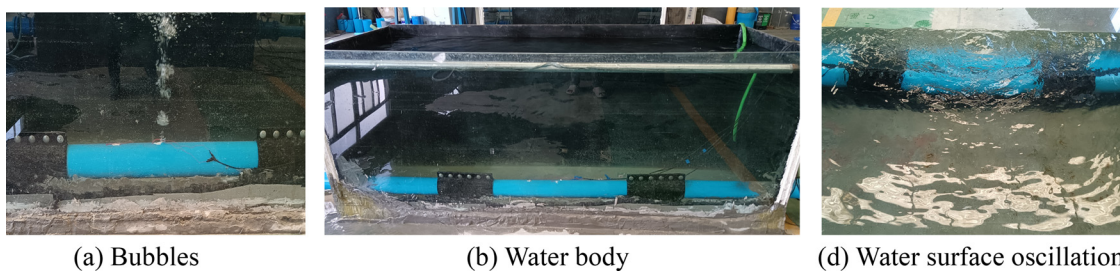


FIG. 9. Phenomenon of water box.

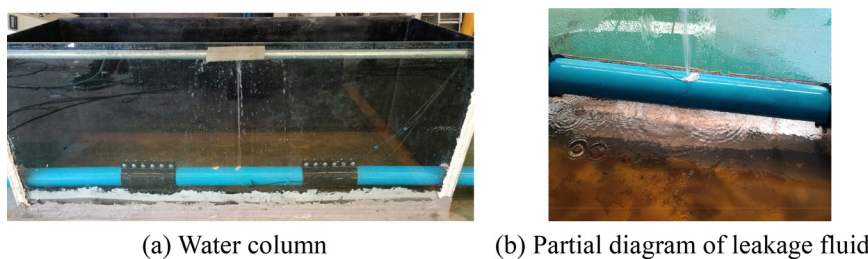


FIG. 10. Phenomenon of air box.

09 January 2025 04:38:34

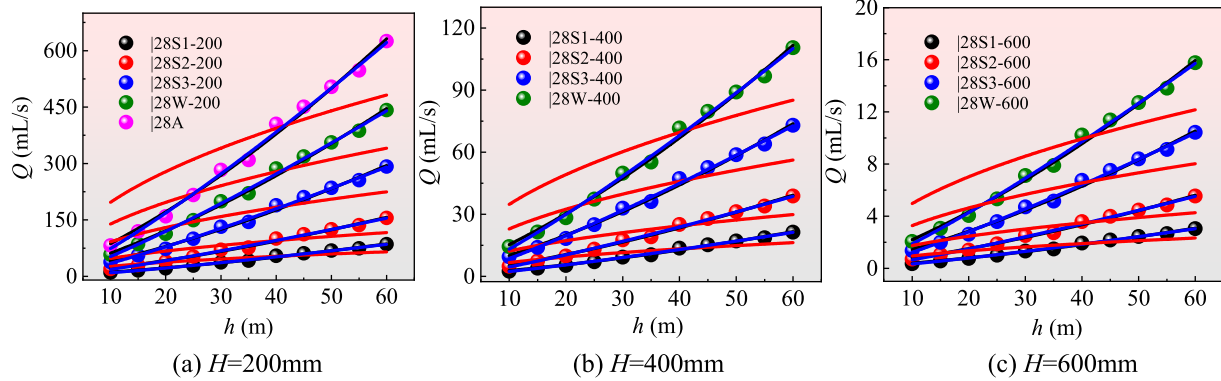


FIG. 11. Leakage flow rate pressure curves of circumferential crack.

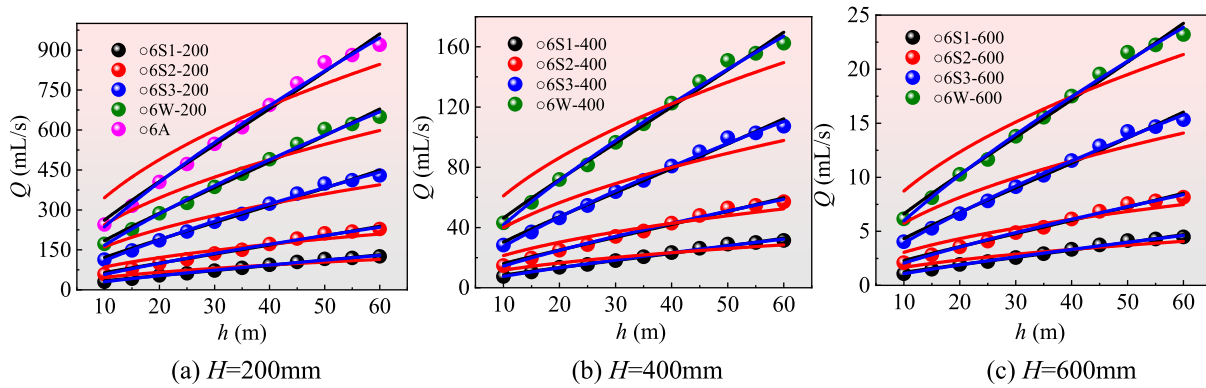


FIG. 12. Leakage flow rate pressure curves of round hole.

fitting results ranges from 0.6014 to 1.2262, which is significantly higher than the conventional index value of 0.5. This can be attributed to the fact that the raw material of the plastic pipe is a high polymer with a low elastic modulus. When subjected to internal pressure, the leakage port undergoes certain deformation, altering the area of the leakage port and resulting in varying leakage flow rates. From this, it is

evident that in the presence of sand, the IWA model and the FAVAD model can be used to approximate the leakage flow rate. However, as the IWA model does not account for the incremental form of the initial area, there is a certain discrepancy with the actual situation. Therefore, the subsequent analysis primarily focuses on the FAVAD model.

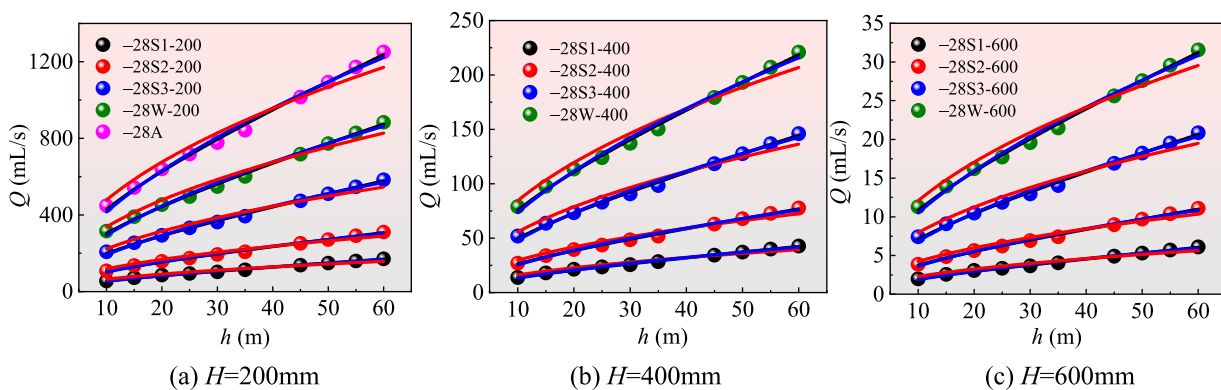


FIG. 13. Leakage flow rate pressure curves of axial crack.

TABLE VI. Fitting results of circumferential crack.

Number	FAVAD					TOR		IWA		
	<i>a</i>	<i>b</i>	<i>m</i>	<i>C_d</i>	<i>R²</i>	<i>C_d√2g</i>	<i>R²</i>	<i>c</i>	<i>α</i>	<i>R²</i>
28S1-200	1.9793	0.1940	0.0274	0.0160	0.9955	8.4105	0.7164	0.5615	1.2262	0.9991
28S2-200	4.0179	0.8106	0.0565	0.0324	0.9944	15.0201	0.7149	1.1717	1.1927	0.9958
28S3-200	7.6465	4.8113	0.1762	0.0617	0.9946	29.0174	0.7261	2.2314	1.1895	0.9960
28W-200	11.7793	8.5559	0.2034	0.0950	0.9949	43.9761	0.7279	3.4412	1.1849	0.9963
28A	16.6869	12.8646	0.2159	0.1345	0.9946	62.2378	0.7279	4.7699	1.1895	0.9989
28S1-400	0.4948	0.0265	0.0150	0.0040	0.9955	2.1027	0.7164	0.1440	1.2203	0.9968
28S2-400	1.0047	0.1299	0.0362	0.0081	0.9944	3.8551	0.7250	0.2930	1.1927	0.9959
28S3-400	1.9122	0.9428	0.1381	0.0154	0.9946	7.2545	0.7261	0.5580	1.1894	0.9960
28W-400	2.9448	1.5200	0.1445	0.0237	0.9949	10.9940	0.7279	0.8603	1.1849	0.9963
28S1-600	0.0702	0.0008	0.0032	0.0006	0.9956	0.3003	0.7159	0.0204	1.2220	0.9968
28S2-600	0.1446	0.0086	0.0167	0.0012	0.9945	0.5511	0.7256	0.04217	1.1908	0.9959
28S3-600	0.2737	0.0981	0.1004	0.0022	0.9946	1.0364	0.7263	0.0799	1.1890	0.9960
28W-600	0.4208	0.3335	0.2219	0.0034	0.9949	1.5704	0.7279	0.1229	1.1848	0.9963

C. Weighted average flow rate histograms

To evaluate the overall level of leakage flow under different leak shapes, Fig. 14 presents a bar chart illustrating the relationship between weighted average leakage flow values and leak types under various pressures. As shown in Fig. 14, under identical outflow medium conditions, the leakage flow rate exhibits an increasing trend on the order of

circumferential cracks, circular holes, and axial cracks, with the highest leakage flow rate occurring in the air medium. Among these, the variation amplitude for circumferential cracks is relatively small, whereas the average leakage flow rate for circular holes and axial cracks demonstrates a clear increasing trend. This is attributed to the fact that under the internal pressure of the water supply pipeline, the circumferential stress

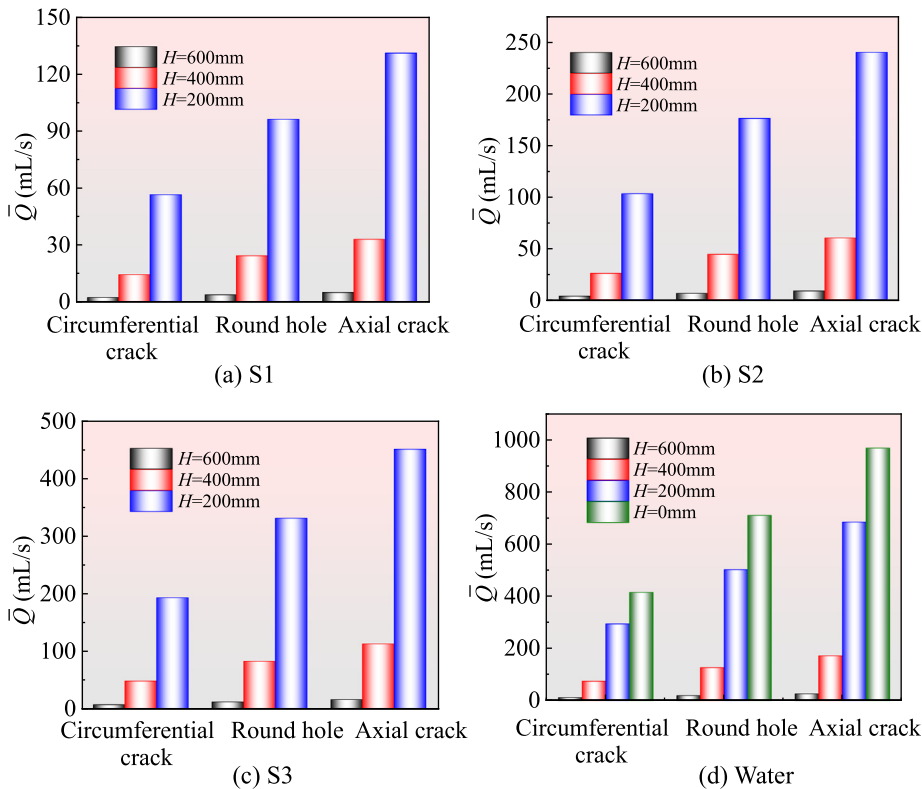


FIG. 14. Weighted average flow rate of different types of leaks.

09 January 2025 04:38:34

exceeds the axial stress, approximately twice as much, with the circumferential stress dictating the area increment of the axial crack and the axial stress dictating the area increment of the circumferential crack. Furthermore, the stress intensity factor for the axial crack is greater than that for the circumferential crack.¹⁸ Under the influence of axial and circumferential stresses, the circular hole deforms into an ellipse, whereas axial cracks tend to open due to the presence of circumferential stress and exhibit significant deformation. Furthermore, due to the Poisson effect, the deformation of circumferential cracks tends to contract under the action of axial stress,^{49,50} leading to a more substantial increase in leakage area for axial cracks compared to circular holes and circumferential cracks, and consequently a more significant increase in flow rate.

D. Factor analysis

The focus of this study is on the influence of medium materials and pipeline burial depth on the leakage flow rate for various types of leaks. To elucidate the influence mechanism of each factor, the subsequent analysis will investigate the impact laws of these two factors on the leakage flow rate.

1. Medium

The changes in leakage flow rate for different types of leaks under various outflow medium materials are depicted in Figs. 15–17. As

shown in the figures, the trend of leakage flow rate changes is similar for each type of leakage port, increasing on the order of S1, S2, S3, W, and A as the medium changes. The slope is small when transitioning from S1 to S2, and then the slope of the curve increases. This is attributed to the gradual increase in permeability, porosity, and particle size of S1, S2, and S3, which results in reduced water flow resistance along the inter-particle pores and accelerated diffusion speed in sand, facilitating easier outflow. Concurrently, the flow field acting on sand particles causes a redistribution of their arrangement, leading to non-uniformity. This results in a highly complex outflow situation, with varying outflow speeds. However, the trend of outflow is evident. As shown in the figures, the greater the applied pressure, the more significant the increase in leakage flow rate. This is because the bulk density of S1, S2, and S3 gradually decreases, resulting in a looser sand structure. As internal pressure increases, the ability of the leakage flow to resist external forces is enhanced, thereby promoting an increase in flow rate. For media W and A, the absence of interactions between sand particles indicates no significant hindering effect is present. Consequently, the maximum leakage flow rate is observed in medium A.

2. Burial depth

The variation in leakage flow rate for different types of leaks at various burial depths (H) is depicted in Figs. 18–20. As shown in the figures, the trend of leakage flow rate changes is similar for each type

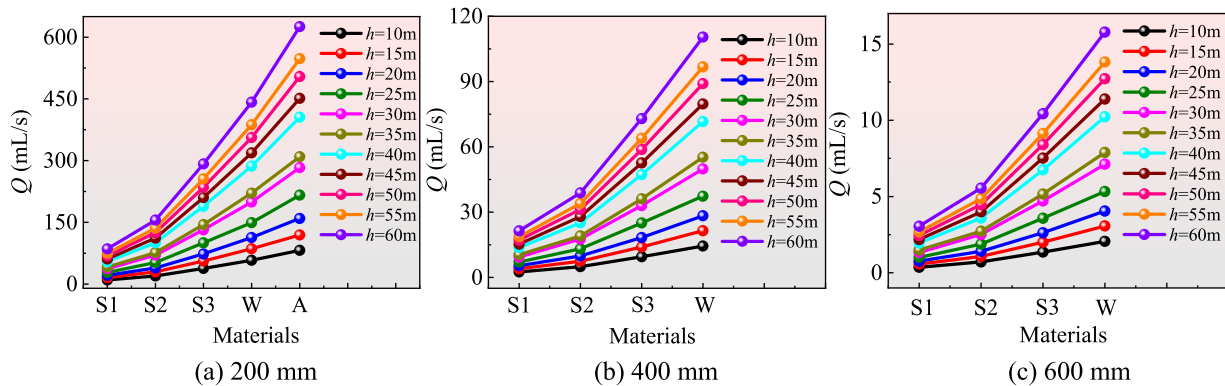


FIG. 15. Changes in leakage flow rate of circumferential crack with different media materials.

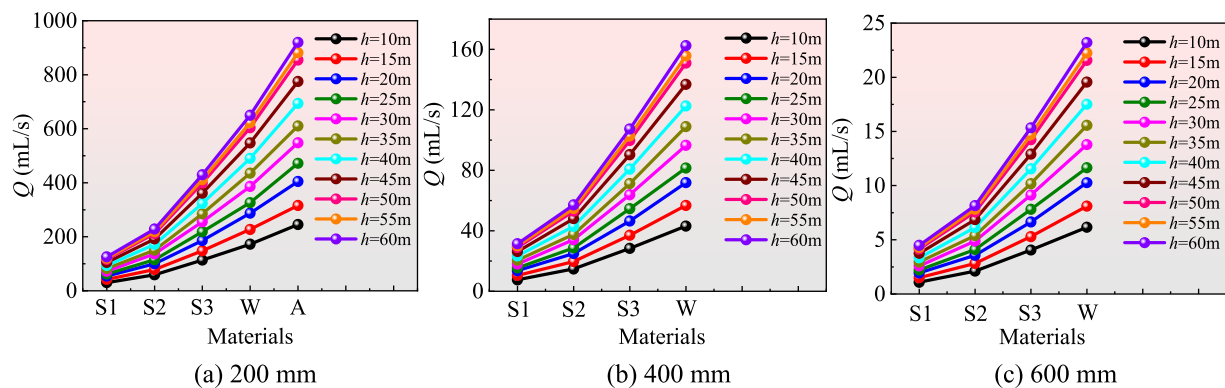


FIG. 16. Changes in leakage flow rate of round hole with different media materials.

09 January 2025 04:38:34

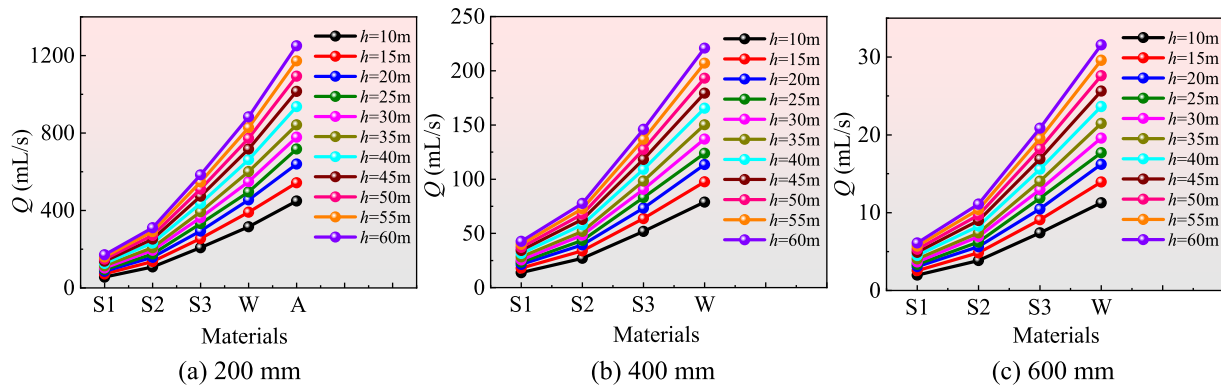


FIG. 17. Changes in leakage flow rate of axial crack with different media materials.

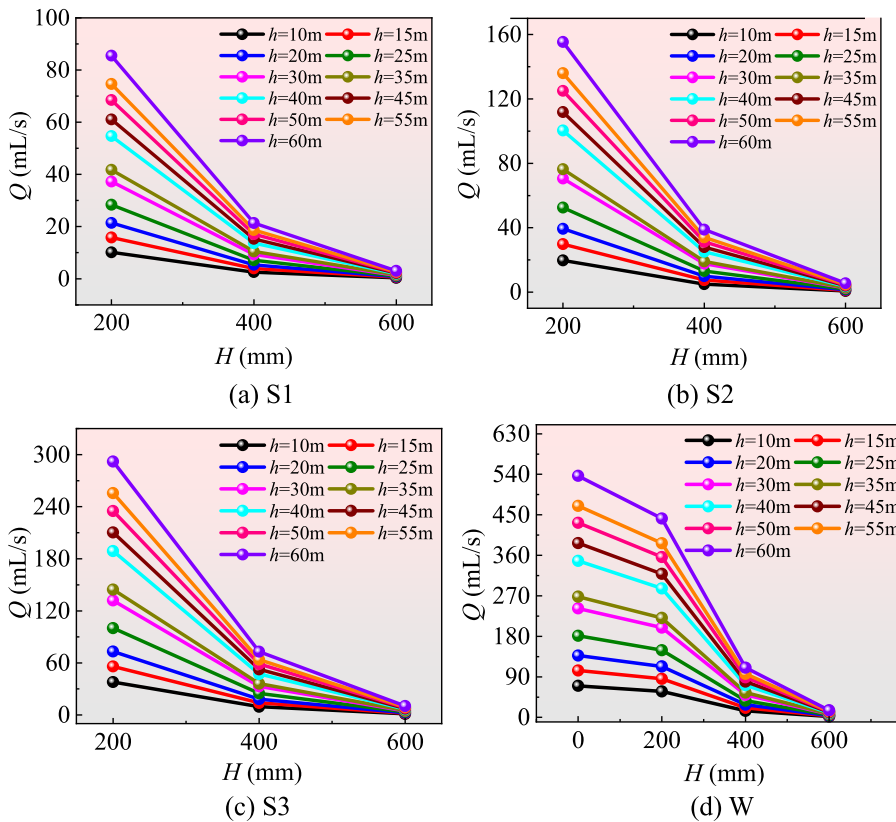


FIG. 18. Changes in flow rate of circumferential crack at different burial depths.

of leak, decreasing with increasing H . When H increases from 200 to 400 mm, the rate of decrease in Q is greater than that when H increases from 400 to 600 mm, and the greater the applied pressure, the more significant the amplitude of this change. This is because, under the same medium, the greater the burial depth, the higher the weight of the overlying sand and the stronger the external resistance to the leaked water flow. When internal pressure is applied, the water flow exhibits a greater ability to resist the external resistance. With increased burial depth, fine sand particles are squeezed between coarse particles,

hindering rapid discharge from the sand body's surface. This further induces a secondary reverse obstruction effect on the water flow, leading to an increased descent speed. This further induces a secondary reverse obstruction effect on the water flow, leading to an increased descent speed. For the W medium, as the burial depth increases, the slope of Q changes from 0 to 200 mm to 200–400 mm, exhibiting larger slopes in the 200–400 mm range and smaller slopes in the 400–600 mm range. The reason for this change is analogous to that observed in sand. The deeper the external water body, the greater its

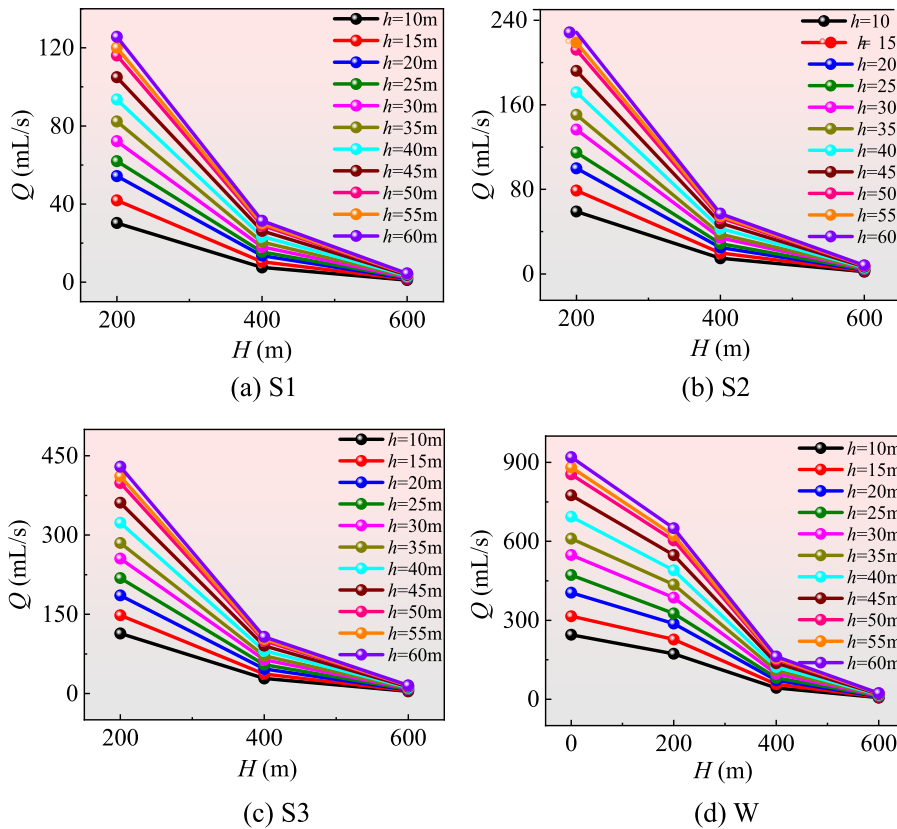


FIG. 19. Changes in flow rate of round hole at different burial depths.

weight, which results in a reduced outflow velocity of water molecule particles. Furthermore, the viscous forces within the water molecules further reduce the outflow velocity of the leakage flow field.

E. FAVAD model evaluation indicators

The focus of this study is to establish the relationship between various factors and the leakage flow rate, thereby evaluating the degree of influence that sand characteristics exert on the leakage flow rate. To achieve this goal, several experiments were conducted on three types of leaks, with each series including three different sand types. Subsequently, based on the relevant results, pressure leakage flow curves were plotted for each sand type, as shown in Figs. 11–13. As shown in the figures, in each type of leakage test, the maximum leakage flow rate occurred in the absence of sand (leakage into the air). Under the same pressure, the leakage flow rate of coarse sand is greater than that of fine sand. The main hypothesis of this study is based on

$$Q = f(h, S). \tag{6}$$

Here, S represents the contribution of sand characteristics. The parameters considered for sand characteristics mainly include the median particle size (d_{50}), permeability coefficient (k), porosity (n), and dry unit weight (γ_d). In the FAVAD model [Eq. (4)], there are primarily two parameters involved, namely the leakage coefficient (C_d) and the slope of the area increment (m). C_d can be used to characterize the magnitude of the leakage intensity, and m can be used to characterize

the rate of increase in the leakage intensity. According to Eq. (4), the calculation formulas for m and C_d are presented as follows:

$$m = \frac{b}{a} \cdot A_0. \tag{7}$$

Here, a represents the FAVAD fitted a value, b represents the FAVAD fitted b value, and A_0 represents the initial leak area

$$C_d = \frac{a}{A_0 \sqrt{2g}}. \tag{8}$$

The calculation results for these parameters are presented in Tables VI–VIII.

Related studies have demonstrated that the properties of sand primarily affect the leakage coefficient, while the impact on the leakage index is negligible.^{51,52} According to the FAVAD model, the increase in leakage area is proportional to the internal pressure [Eq. (3)], and due to the certain correlation between C_d and m , it can be inferred that the presence of sand will inevitably affect the growth rate of the leakage area m . Following the approach in the literature,⁴² if all other experimental characteristics are kept constant and only sand characteristics and internal pressure are considered in the analysis, the relationship between Q , C_d , m , and sand parameters can be assumed to be linear. Subsequently, the permeability coefficient (k) and the sand self-weight stress ($\gamma_d H$) will be considered as representative parameters for further linear regression analysis to determine the variation law of the leakage flow rate with key sand characteristic parameters.

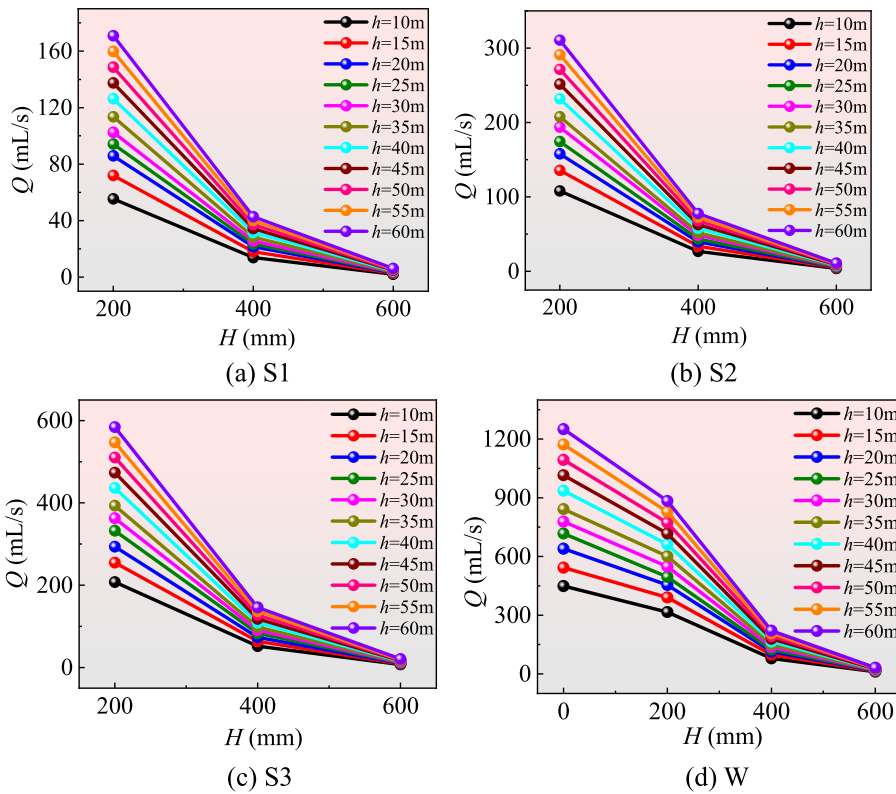


FIG. 20. Changes in flow rate of axial crack at different burial depths.

1. Leakage area-pressure slope values

The variation in leakage area and pressure slope value (m) for each type of leak is depicted in Figs. 21 and 22. From Fig. 21, it is evident that m increases with the increase in k , and the rate of increase for each leakage type is similar, exhibiting a relatively uniform change.

This is because, as k increases, the fluid becomes easier to discharge, and the movement of the fluid causes the sand around the leak to migrate, thereby reducing the degree of constraint the sand exerts on the deformation at the leak. Consequently, the deformation of the leak area becomes easier, resulting in an increase in the leak area and a corresponding increase in the value of m . From Fig. 22, it is evident that

TABLE VII. Fitting results of round hole.

Number	FAVAD					TOR		IWA		
	a	b	m	C_d	R^2	$C_d\sqrt{2g}$	R^2	c	α	R^2
○6S1-200	2.7649	0.3252	0.0329	0.0223	0.9911	14.7391	0.8793	4.6938	0.8100	0.9954
○6S2-200	7.5633	1.8311	0.0678	0.0610	0.9914	27.063	0.8922	9.5480	0.7824	0.9954
○6S3-200	10.5941	7.9992	0.2114	0.0854	0.9917	50.9359	0.8939	18.1937	0.7791	0.9955
○6W-200	12.6880	11.0592	0.2441	0.1023	0.9915	77.2218	0.8961	28.1263	0.7738	0.9952
○6A	16.1017	14.8962	0.2590	0.1298	0.9916	109.2837	0.8962	39.7807	0.7740	0.9954
○6S1-400	0.6426	0.0413	0.0180	0.0052	0.9911	3.6849	0.8793	1.1731	0.8101	0.9954
○6S2-400	1.9504	0.3026	0.0434	0.0157	0.9914	6.7658	0.8921	2.3870	0.7824	0.9954
○6S3-400	6.0137	3.5580	0.1657	0.0485	0.9917	12.6288	0.8932	4.5481	0.7791	0.9955
○6W-400	7.7773	4.8173	0.1734	0.0627	0.9915	19.3055	0.8961	7.0311	0.7738	0.9952
○6S1-600	0.3291	0.0045	0.0038	0.0027	0.9910	0.5265	0.8793	0.1677	0.8099	0.9954
○6S2-600	0.7076	0.0505	0.0200	0.0057	0.9914	0.9668	0.8924	0.3416	0.7820	0.9954
○6S3-600	1.2881	0.5540	0.1204	0.0104	0.9916	1.8192	0.8938	0.6497	0.7791	0.9955
○6W-600	2.8942	2.7525	0.2663	0.0233	0.9915	2.7579	0.8960	1.0043	0.7739	0.9952

TABLE VIII. Fitting results of axial crack.

Number	FAVAD					TOR		IWA		
	<i>a</i>	<i>b</i>	<i>m</i>	<i>C_d</i>	<i>R²</i>	<i>C_d√2g</i>	<i>R²</i>	<i>c</i>	<i>α</i>	<i>R²</i>
-28S1-200	5.9934	0.9869	0.0461	0.0483	0.9971	20.3615	0.9547	12.1155	0.6412	0.9932
-28S2-200	8.6441	2.9298	0.0949	0.0697	0.9970	37.4207	0.9666	24.8627	0.6113	0.9930
-28S3-200	12.7116	13.4372	0.2960	0.1025	0.9972	70.4378	0.9682	47.4924	0.6073	0.9930
-28W-200	14.8887	18.1683	0.3417	0.1200	0.9967	106.8061	0.9699	73.5636	0.6015	0.9925
-28A	18.8340	24.3934	0.3626	0.1519	0.9968	151.1497	0.9699	103.8897	0.6021	0.9927
-28S1-400	0.7969	0.0717	0.0252	0.0064	0.9970	5.0906	0.9547	3.0295	0.6412	0.9932
-28S2-400	3.7401	0.8124	0.0608	0.0302	0.9970	9.3550	0.9667	6.2160	0.6113	0.9930
-28S3-400	8.8847	7.3593	0.2319	0.0716	0.9972	17.6092	0.9682	11.8736	0.6073	0.9930
-28W-400	5.3070	4.6021	0.2428	0.0428	0.9967	26.7018	0.9699	18.3912	0.6015	0.9925
-28S1-600	0.3970	0.0076	0.0054	0.0032	0.9970	0.7275	0.9544	0.4320	0.6417	0.9932
-28S2-600	0.9468	0.0946	0.0280	0.0076	0.9970	1.3367	0.9667	0.8884	0.6112	0.9929
-28S3-600	2.2063	1.3285	0.1686	0.0178	0.9972	2.5157	0.9682	1.6963	0.6073	0.9930
-28W-600	2.7373	3.6447	0.3728	0.0221	0.9967	1.4294	0.9699	2.6281	0.6014	0.9925

m decreases with the increase in $\gamma_d H$. The variation pattern of *m* values for different types of leaks at various burial depths is consistent, exhibiting roughly equal slopes. However, the *m* values in S1 and S2 media are lower than those in S3. This is because, the larger the $\gamma_d H$, on the

one hand, it increases the compactness of the sand, and on the other hand, it also increases the external load—the self-weight of the sand—which significantly suppresses the increase in leakage area and deformation, thereby causing a decrease in the *m* value. However, S3 has a

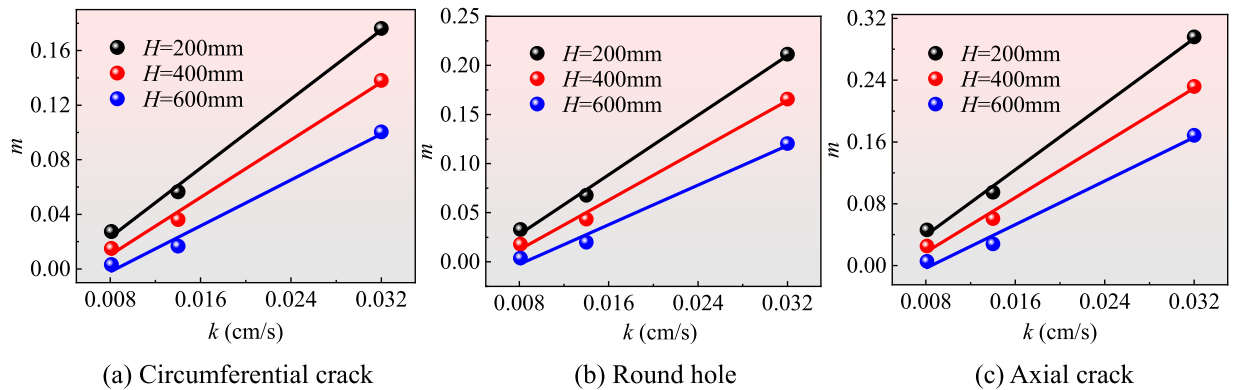


FIG. 21. Leakage area-pressure slope values and permeability coefficient curves.

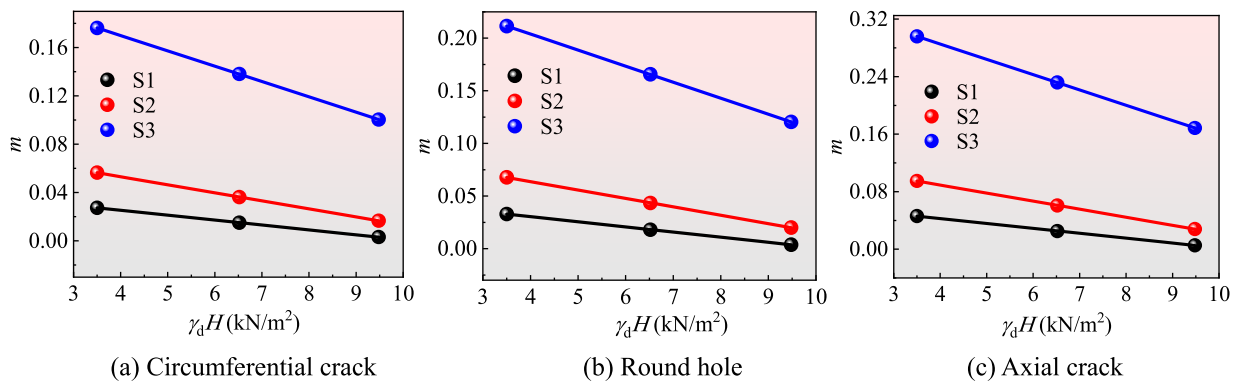


FIG. 22. Leakage area-pressure slope values and sand self-weight stress curves.

09 January 2025 04:38:34

TABLE IX. Fitting formula for the leakage area-pressure slope values.

Circumferential crack		Round hole		Axial crack	
Relational equation	R^2	Relational equation	R^2	Relational equation	R^2
$m = 6.3253k - 0.0274$	0.9971	$m = 7.5879k - 0.0328$	0.9971	$m = 10.6238k - 0.0459$	0.9971
$m = 5.2702k - 0.0319$	0.9940	$m = 6.3238k - 0.0383$	0.9940	$m = 8.8492k - 0.0536$	0.9940
$m = 4.2035k - 0.0357$	0.9878	$m = 5.0424k - 0.0429$	0.9878	$m = 7.0586k - 0.0560$	0.9877
$m = -0.0041\gamma_d H + 0.0415$	0.9999	$m = -0.0049\gamma_d H + 0.0499$	0.9999	$m = -0.0068\gamma_d H + 0.0698$	0.9999
$m = -0.0067\gamma_d H + 0.0797$	0.9999	$m = -0.0080\gamma_d H + 0.0957$	0.9999	$m = -0.0112\gamma_d H + 0.1340$	0.9999
$m = -0.0127\gamma_d H + 0.0415$	0.9999	$m = -0.0152\gamma_d H + 0.2647$	0.9999	$m = -0.0213\gamma_d H + 0.3706$	0.9999

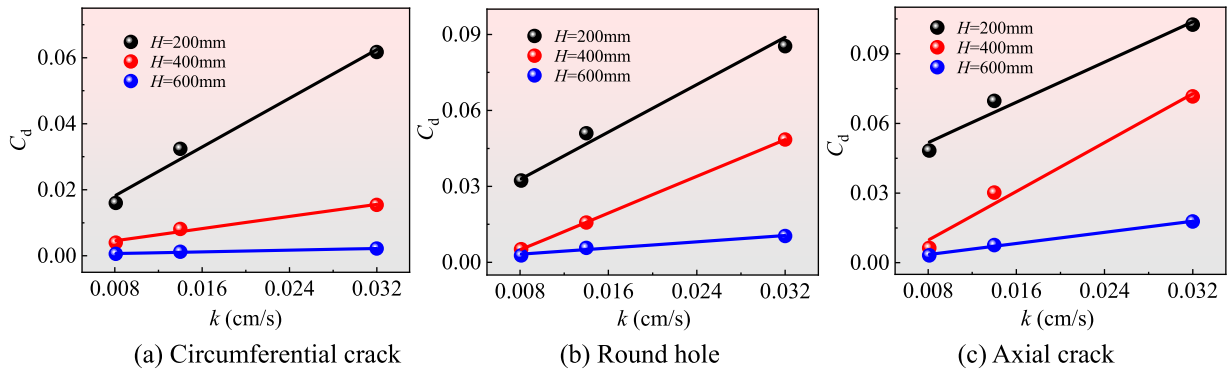


FIG. 23. Leakage coefficient and permeability coefficient curves.

higher permeability coefficient than S1 and S2, hence the m value is relatively large. The fitting formula for the m value of each leakage type is presented in Table IX.

2. Leakage coefficient

The variation in leakage coefficient (C_d) values for each type of leak is depicted in Figs. 23 and 24. From Fig. 23, it is evident that C_d increases with the increase in k , and the changes across various types of leaks are roughly similar. When H is 600 mm, the increase in C_d is relatively small for all three types of leaks. This is because, as k increases, the

fluid becomes easier to discharge. It is evident that C_d is not only related to the type and size of the leakage port but also to the characteristics of the sand surrounding the leakage port. Furthermore, the larger H , the longer the resistance path of the leaked fluid outflow, and the magnitude of the increase in leakage intensity is suppressed to a certain extent. As shown in Fig. 24, C_d decreases with the increase in $\gamma_d H$, and the variation pattern of C_d values for different types of leaks at various burial depths is roughly consistent. However, the absolute value of the slope for the circumferential crack (corresponding to S3) is greater than that of the circular hole and axial crack. This may be attributed to the tendency of circumferential stress to elongate the circumferential crack,

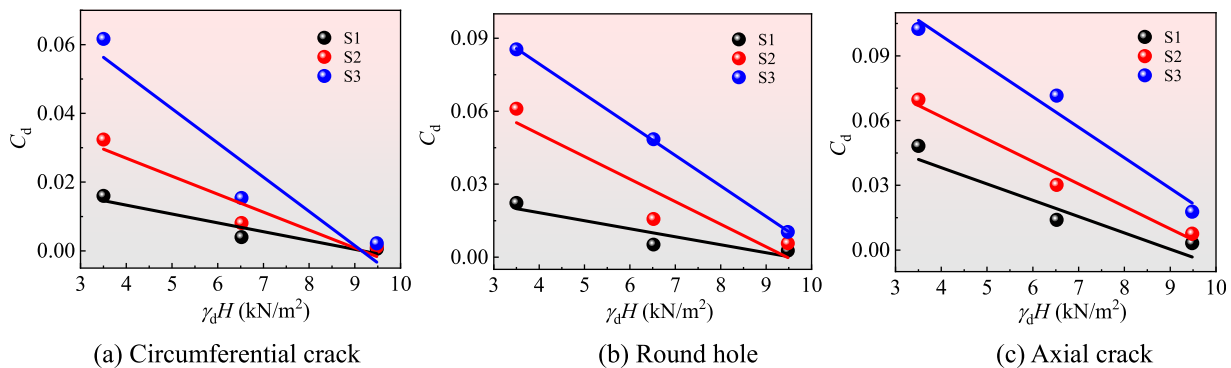


FIG. 24. Leakage coefficient and sand self-weight stress curves.

09 January 2025 04:38:34

TABLE X. Fitting formula for leakage coefficient.

Circumferential crack		Round hole		Axial crack	
Relational equation	R^2	Relational equation	R^2	Relational equation	R^2
$C_d = 1.8455k + 0.0034$	0.9850	$C_d = 2.3393k + 0.0141$	0.9850	$C_d = 2.1634k + 0.0345$	0.9735
$C_d = 0.4603k$	0.9847	$C_d = 1.8142k - 0.0096$	0.9999	$C_d = 2.6278k - 0.0113$	0.9833
$C_d = 0.0643k$	0.9802	$C_d = 0.3079k$	0.9754	$C_d = 0.6005k - 0.0013$	0.9965
$C_d = -0.0026\gamma_d H + 0.0236$	0.9092	$C_d = -0.0033\gamma_d H + 0.0314$	0.9092	$C_d = -0.0076\gamma_d H + 0.0685$	0.9092
$C_d = -0.0052\gamma_d H + 0.0479$	0.9094	$C_d = -0.0093\gamma_d H + 0.0877$	0.9094	$C_d = -0.0104\gamma_d H + 0.1034$	0.9777
$C_d = -0.0100\gamma_d H - 0.0912$	0.9098	$C_d = -0.0125\gamma_d H - 0.1296$	0.9998	$C_d = -0.0142\gamma_d H + 0.1560$	0.9744

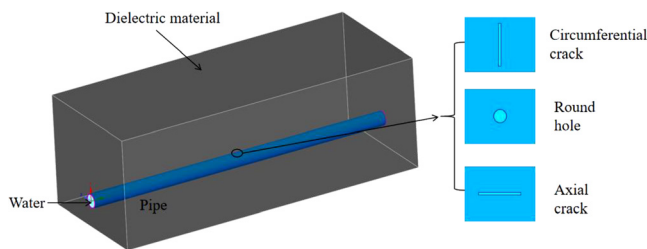


FIG. 25. Geometric model.

and, due to the Poisson effect, a certain decrease in its width direction, leading to a rapid decrease in its leakage strength. Therefore, the decrease in the C_d value for the circumferential crack is greater than that for the circular hole and axial crack. The fitting formulas for C_d values of each leakage type are presented in Table X.

IV. ANSYS FLUENT SIMULATION

A. Model

1. Geometry

ANSYS Fluent software is currently the mainstream commercial CFD software, which can be used to solve engineering problems involving fluids, heat transfer, and mass transport. The establishment and analysis of the finite element model for the single-point leakage pipe section in this study were completed on the ANSYS Workbench platform. First, SpaceClaim software is used to establish a pipeline model, on which circumferential cracks, circular holes, and axial cracks

are introduced. The fluid domain is generated using the volume extraction function, and the external sand area is generated using the shell function. The geometric model, as shown in Fig. 25, is then imported into the ANSYS Workbench software calculation platform.

2. Coupling module

The model establishment is primarily divided into module A: fluid flow, module B: static structural,^{53,54} and the overall coupled analysis of the model. Since the strain and stress changes at the pipeline leakage are induced by changes in the fluid pressure inside the pipeline, module A can be used to obtain the flow velocity, pressure, and other parameters of the internal fluid. Module B applies the results from module A to the solid pipeline to obtain the changes in various physical parameters at the pipeline leakage, thereby determining the pressure, stress, strain, and area change laws of the leakage. In the modeling process, the settings for the flow coefficient are as follows: The $k - \epsilon$ model, in its realizable form with the standard wall function, is selected for the turbulence model; the turbulence intensity is set to 5%; the fluid property is set to water; and the pipeline’s water inlet is designated as a pressure inlet.^{55–58} Based on the pressure input for the experimental water supply pipeline, the iteration number for the entire flow model is set to 200. This modeling analysis employs the polyhedral meshing method for discretization, offering higher efficiency compared to tetrahedral and hexahedral meshing methods. This method facilitates multi-core parallel acceleration, fully utilizes hardware performance, enhances computational accuracy, and reduces computation time. The surface and volume meshes are detailed in Fig. 26.

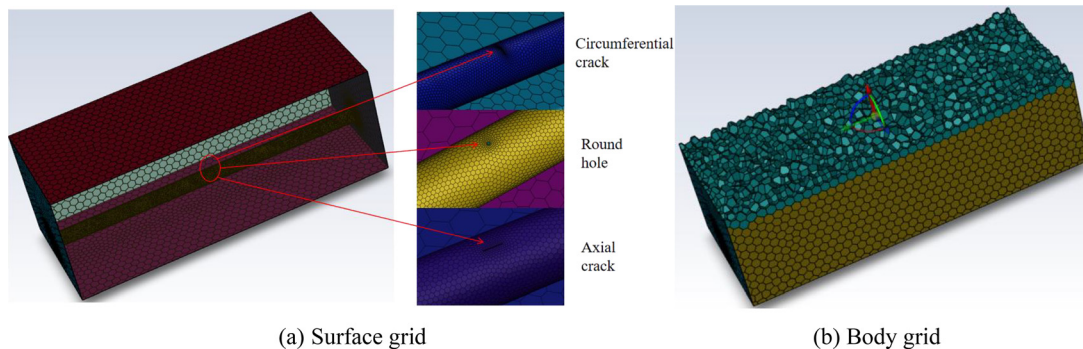


FIG. 26. Polyhedral grid.

09 January 2025 04:38:34

B. Model validation

1. Verification of grid independence

The form and quality of the grid significantly impact the flow field analysis, which in turn affects Fluent’s simulation results. The degree of grid density plays a crucial role in simulating turbulent flow fields. The important purpose of grid quality assessment is to determine the appropriate grid structure type and the number of elements for model calculations. High-quality computational grids are a prerequisite for accurately simulating flow fields.⁵⁹ Taking the prefabricated round hole condition as an example, in this section, we employed the same grid partitioning method to compare the distribution of velocity contour lines in the leakage flow field across various grid numbers. The results are presented in Fig. 27. As shown in the figure, the convergence trend of the solutions is consistent across different grid numbers. When the number of grid nodes exceeds 1 236 824, the contour distribution of flow velocity in the flow field remains essentially unchanged. Furthermore, Fig. 28 shows the variation curve of the velocity (v_0) at the leakage port with the number of grids. As

shown in the figure, as the number of grid nodes increases beyond 1 236 824, the convergence solution v_0 of numerical calculation is 25 m/s. Therefore, when 1 236 824 is used, it can be considered that the numerical solution is independent of the number of grids.

2. Analysis of grid convergence index

The following section introduces the grid convergence index (GCI) for further discussion and analysis of grid independence. According to the literature,^{60–63} grid convergence error is defined as

$$\varepsilon = \frac{f_1 - f_2}{f_1} \tag{9}$$

Here, f_1 and f_2 are the fine grid convergence solution and the coarse grid convergence solution, respectively. f can be any quantity of concern and is taken as v_0 here. The grid refinement ratio is defined as

$$r_{k,k+1} = \frac{h_k}{h_{k+1}} \tag{10}$$

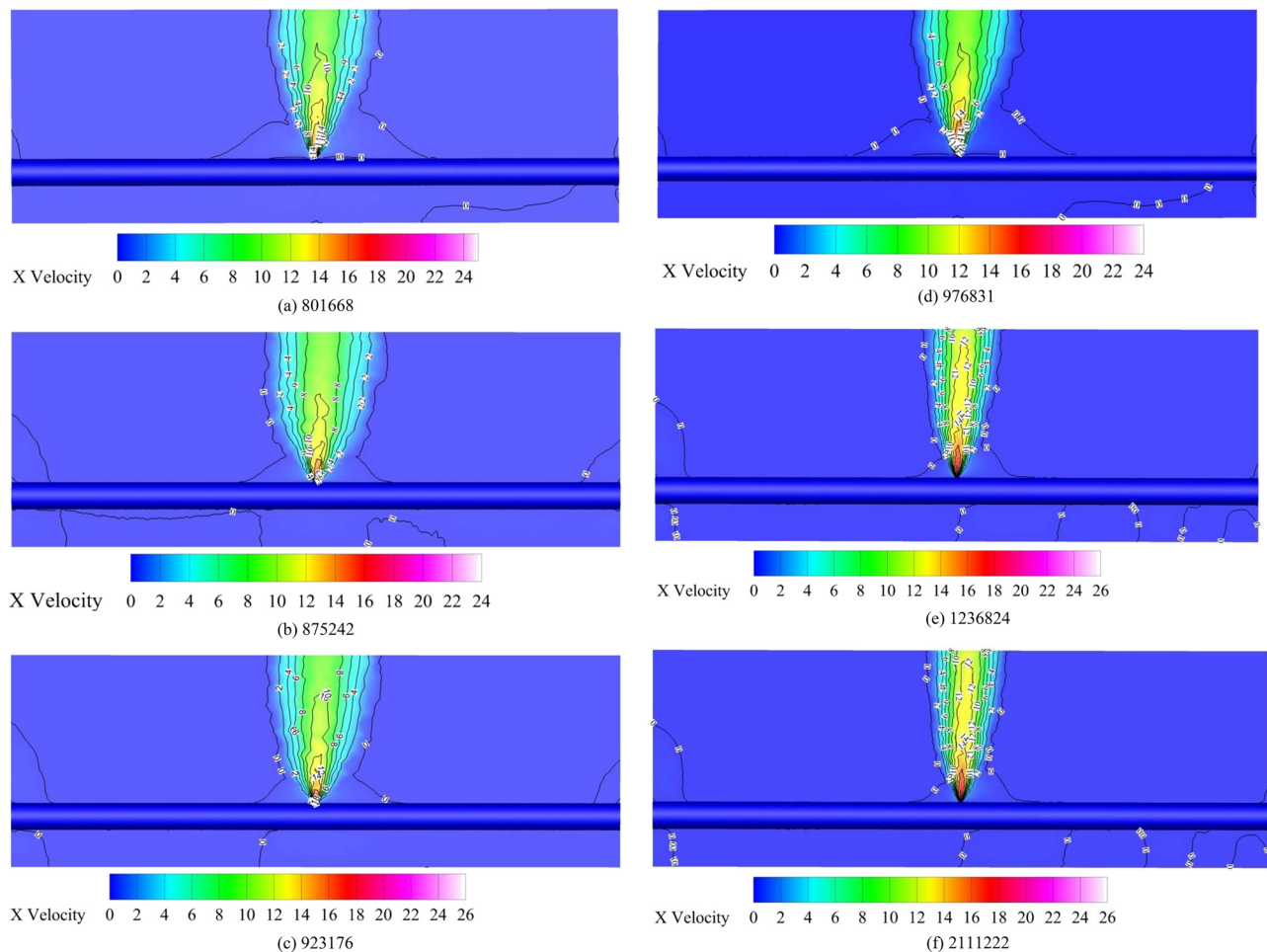


FIG. 27. The distribution of velocity contour lines.

09 January 2025 04:38:34

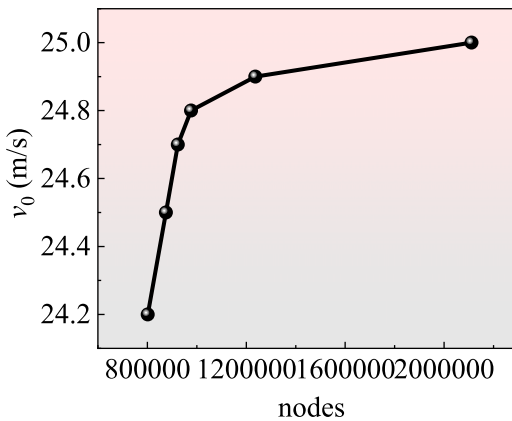


FIG. 28. Curve of leakage velocity changing with the number of grid nodes.

In the formula, h_k is the average spacing between each grid, calculated by

$$h_k = \sqrt[3]{\frac{\sum_{i=1}^{N_k} \Delta V_i}{N_k}} \tag{11}$$

Here, ΔV_i is the volume of each grid cell; and N_k is the total number of nodes per grid set. For the same physical model, the number of nodes in the grid varies, but the total volume remains constant. The grid refinement ratio can be simplified as

$$r_{k,k+1} = \frac{h_k}{h_{k+1}} = \sqrt[3]{\frac{N_{k+1}}{N_k}} \tag{12}$$

The grid convergence index (GCI) is defined as

$$GCI = F_s \frac{|\varepsilon|}{r^p - 1} \tag{13}$$

Here, F_s is the safety factor, and when using two sets of grids to estimate GCI , the value of F_s is 3; When using 3 or more sets of grids to estimate GCI , F_s is taken as 1.25, p is the convergence exponent, taken as 1.97.

The calculation results for GCI are presented in Table XI. It can be seen from the table that the GCI for two consecutive sets of grid calculations, 976 831 and 1 236 824, is 2.99% and 1.19%, respectively, both less than 3%, meeting the grid convergence index criterion.⁶³

TABLE XI. GCI results of v_0 under different structured grids.

Number	r	v_0 (m/s)	ε	$GCI/\%$
801 668	1.030	24.2	0.012 24	25.79
875 242	1.018	24.5	0.008 10	28.40
923 176	1.019	24.7	0.004 03	13.34
976 831	1.082	24.8	0.004 02	2.99
1 236 824	1.195	24.9	0.004 00	1.19
2 111 222	...	25.0

This indicates that when the number of grid nodes is 976 831, the calculated values of numerical simulations are independent of the number of grids. To achieve higher accuracy, this study employed a grid size of 1 236 824. Adopting the same approach, the number of mesh nodes for the prefabricated circumferential crack and axial crack were 1 231 292 and 1 220 766, respectively.

3. Flow velocity cloud diagram

Taking the working condition under a water pressure of 0.4 MPa as an example, the flow velocity distribution of the leaked fluid at each leakage port is shown in Figs. 29–31 through fluent modeling analysis. As shown in the figures, the presence of a leak causes the leakage fluid to overflow, and the area at the leak is much smaller than the diameter of the pipeline. According to the Bernoulli equation, assuming the mechanical energy of the fluid is conserved, the sum of the gravitational potential energy, dynamic potential energy, and pressure potential energy of an ideal liquid remains constant. Due to the low pressure at the leak, the fluid flow velocity at the leak is significantly higher than that in a normal pipeline, with the maximum flow velocity occurring at the center of the leak. The velocity distribution of the leaked fluid at each leak is approximately in the shape of an inverted cone, with a relatively high velocity of around 25 m/s in air medium and a relatively low velocity of around 5 m/s in sand medium.

4. Pipeline deformation cloud diagram

Due to the existence of leakage ports, the water pressure inside the pipeline changes and is not uniformly distributed. In different surrounding media, the outer surface of the pipeline will also bear certain external forces. Therefore, in the process of coupling analysis, the external forces generated by the flow field interference inside and outside the pipeline are considered and applied to the pipeline structure. Through coupling analysis, the deformation characteristics of pipelines under various leakage forms are shown in Figs. 32–34. In air and sand media, the maximum deformation occurs at the center of the leakage port, while in water media, the maximum deformation occurs at the bottom of the pipeline. This may be due to the tension of the external water body, which limits the deformation of the pipeline leakage port. In sand media, the flow changes of the sand water mixture formed by the intrusion of the leakage fluid into the sand are irreversible, and the deformation of the pipeline on the outer surface is somewhat random due to the complex effects of the sand water mixture. Overall, the final deformation of each leak is approximately elliptical, with the order of deformation being: circumferential crack < circular leak < axial crack. Figure 35 shows the comparison between the finite element analysis and experimental results under the 0.4 MPa working condition. It can be seen from the figure that the two agree well, indicating that the finite element analysis calculation is accurate, reliable, and has high accuracy.

C. Finite element parameter expansion analyzes

As shown in Table XII, to assess the influence of various parameters on leakage characteristics, ANSYS Fluent finite element software was utilized for parameter extension analysis based on the experimental results. When one parameter was varied while the others remained constant, the results for the m values

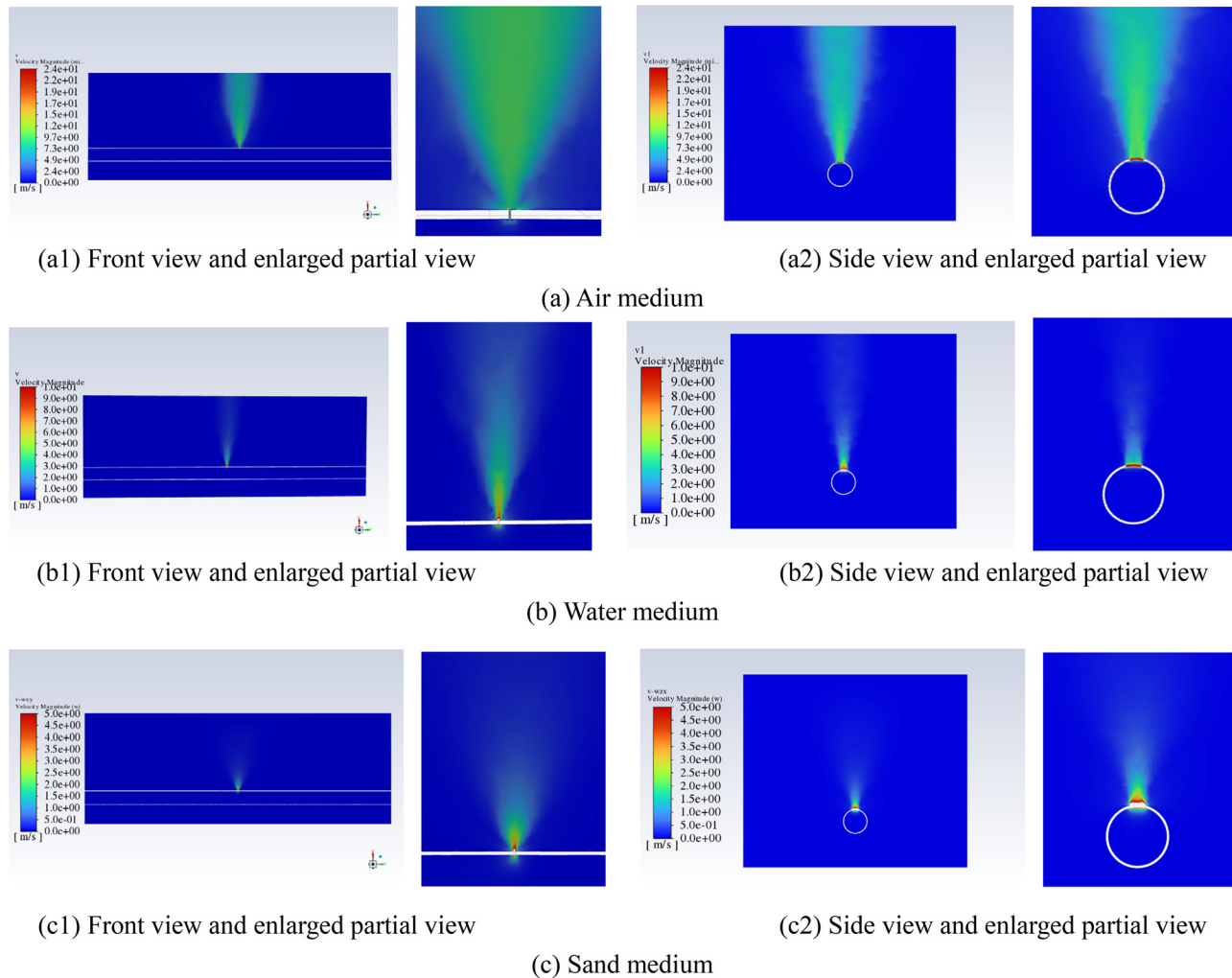


FIG. 29. Flow velocity cloud diagram of fluid leaking from circumferential crack.

are presented in Figs. 36–38. As shown in the figures, for circumferential cracks, except for the TOR model, m increases approximately linearly with the increase in D , increases approximately exponentially with the increase in $l(d)$, and decreases approximately exponentially with t and E . All other models show good agreement with the finite element results. For circular leaks and axial cracks, neither the TOR model nor the IWA model aligns well with the finite element method, while only the FAVAD model remains consistent with both the finite element method and the experimental results. This may be attributed to the fact that both the TOR model and the IWA model disregard the influence of pipeline leak deformation, leading to significant errors in the calculation process.

V. IMPROVED FAVAD MODEL

The existing FAVAD model to some extent explains why the leakage index is higher than 0.5, but this model only accounts for elastic deformation and neglects plastic deformation. The model is entirely

based on empirical assumptions and overlooks the physical derivation process. Its utility for guiding leakage control is very limited. The model can substantiate a range of leakage index values from 0.5 to 2.5, which does not fully account for the problem reported in the literature that the leakage index ranges from 0.36 to 2.95. It fails to effectively simulate the relationship between axial crack leakage flow rate and water head in fixed pipelines. Therefore, this section focuses on enhancing the FAVAD model, analyzing the variations in the leakage index using this model, and investigating leakage control measures. The influence of various factors is not an isolated action, but the result of their joint interaction, and it is not a simple linear relationship. The leakage behavior within sand is more complex. Based on relevant physical quantities and the FAVAD model and incorporating experimental and finite element data, this paper further explores the theoretical formulations. The essence of the FAVAD model is presented in

$$Q = C_d A_r \sqrt{2gh}. \tag{14}$$

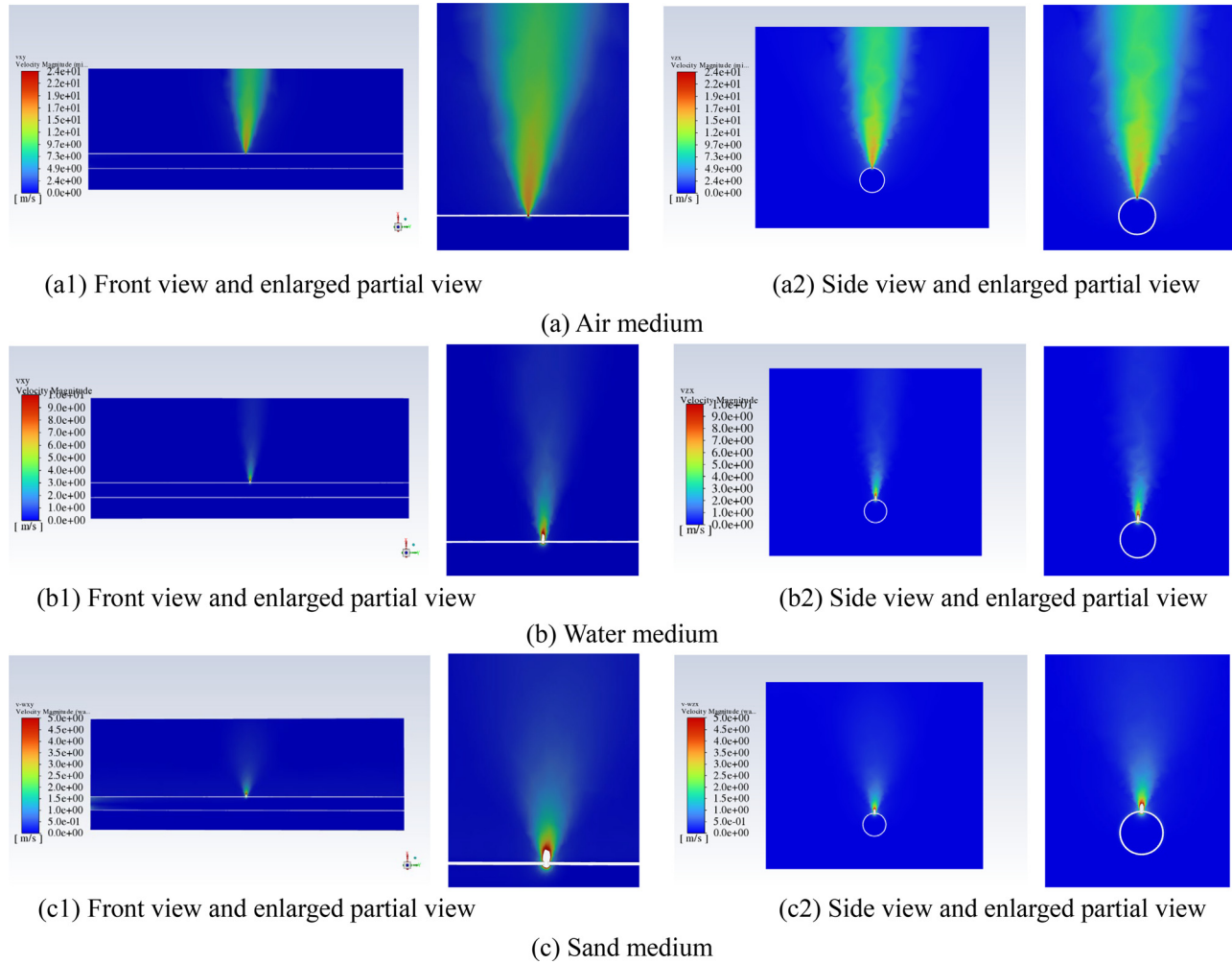


FIG. 30. Flow velocity cloud diagram of fluid leaking from round hole.

Previous studies⁵⁰ have demonstrated that the stress analysis of pressure pipelines is depicted in Fig. 39 and the corresponding calculation formulas are presented in Eqs. (15)–(17). Among them, \vec{i}_c , \vec{i}_l , and \vec{i}_r are the unit vectors in the circumferential, axial, and radial directions, respectively,

$$\vec{\sigma}_{cd} = \frac{\rho g h r_{in}^2 \left(1 + \frac{r_{ex}^2}{r^2}\right)}{r_{ex}^2 - r_{in}^2} \vec{i}_c, \quad (15)$$

$$\vec{\sigma}_{ld} = \frac{\rho g h r_{in}^2}{r_{ex}^2 - r_{in}^2} \vec{i}_l, \quad (16)$$

$$\vec{\sigma}_{rd} = \frac{\rho g h r_{in}^2 \left(1 - \frac{r_{ex}^2}{r^2}\right)}{r_{ex}^2 - r_{in}^2} \vec{i}_r. \quad (17)$$

Among them, σ_{cd} is the circumferential stress, measured in Pa; σ_{ld} is the axial stress, measured in Pa; σ_{rd} is the radial stress, measured in Pa. ρ is the density of water, measured in kg/m^3 ; g is the acceleration

due to gravity, measured in m/s^2 ; h is total head of internal pressure, measured in m; r_{in} is the radius of the inner wall of the pipeline, measured in m; r_{ex} is the radius of the outer wall of the pipeline, measured in m; and r is the calculated radius at any point on the pipeline, measured in m. Integrate the stresses along the wall thickness and divide by the total thickness to obtain their respective average values; note that the average value of axial stress remains constant and equals itself. Their expressions are presented in

$$\bar{\sigma}_{cd} = \frac{\rho g h D_{in}}{2\delta} \vec{i}_c, \quad (18)$$

$$\bar{\sigma}_{rd} = \frac{-\rho g h D_{in}}{D_{in} + D_{ex}} \vec{i}_r, \quad (19)$$

$$\bar{\sigma}_{ld} = \bar{\sigma}_{ld} = \frac{\rho g h D_{in}^2}{4(\delta^2 + D_{in}\delta)} \vec{i}_l. \quad (20)$$

Among them, $\bar{\sigma}_{cd}$ is the average value of circumferential stress, measured in Pa; D_{in} is the diameter of the inner wall of the pipe,

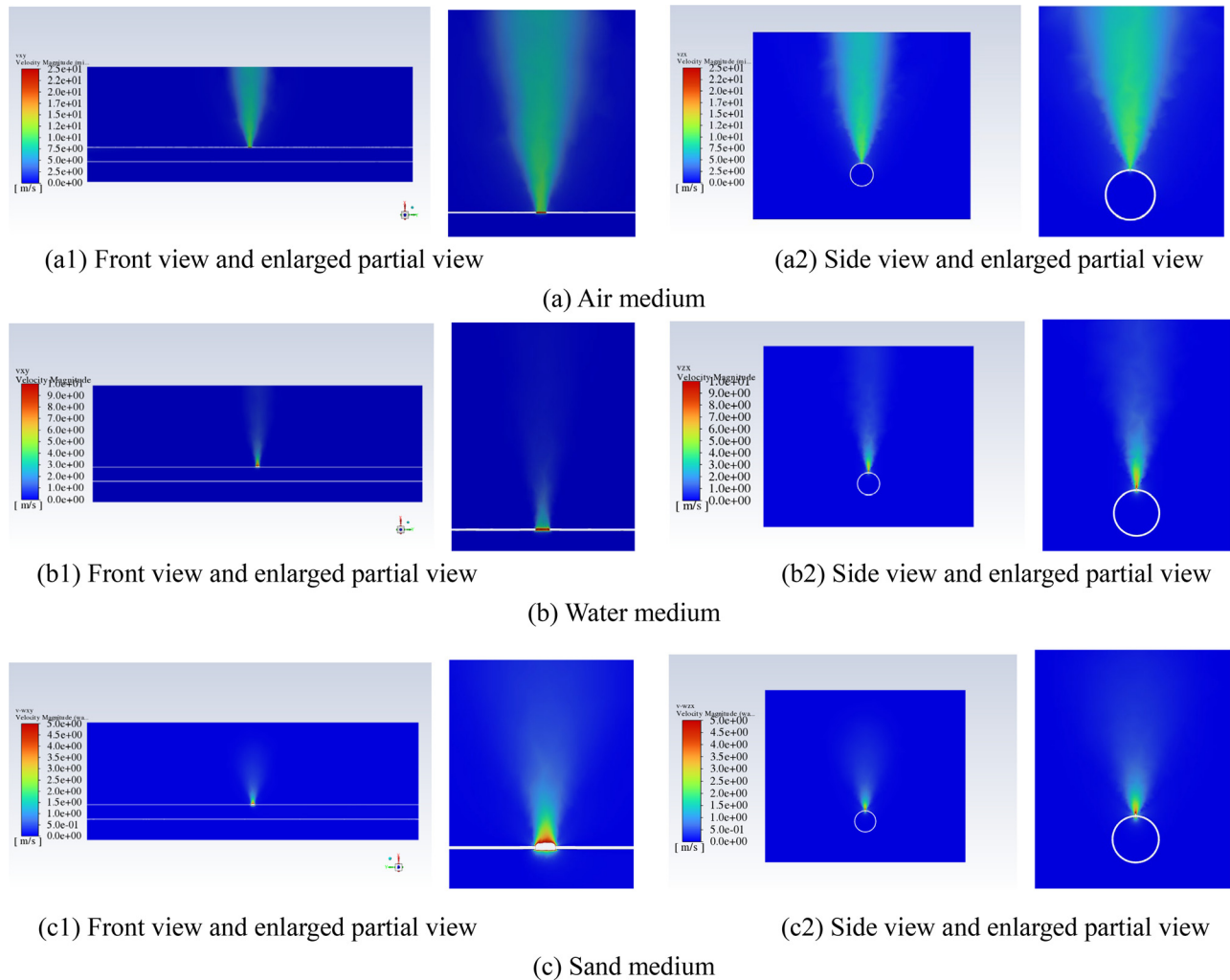


FIG. 31. Flow velocity cloud diagram of fluid leaking from axial crack.

measured in m; δ is the thickness of the pipe wall, measured in m; $\bar{\sigma}_{rd}$ is the average value of radial stress, measured in Pa; D_{ex} is the diameter of the outer wall of the pipe, measured in m; and $\bar{\sigma}_{ld}$ is the average value of axial stress, measured in Pa.

Analysis reveals that among the three stresses, the circumferential stress is the highest and the radial stress is the lowest. Due to the fact that the thickness of the pipe wall in the water supply pipeline is significantly smaller than the diameter of the pipeline, the axial stress is approximately half of the circumferential stress. Based on the experimental phenomena described in Sec. III A, it can be inferred that in some cases, the conditions for calculating the leakage expansion displacement using EPRI⁶⁴ are no longer satisfied. Therefore, when there are leakage points on the pipeline wall and pressurized water within the pipeline, the circular leakage is assumed to expand in an elliptical shape, the axial crack is assumed to expand along the short axis of the ellipse, and the circumferential crack is assumed to expand only along the short side of the rectangular shape (ignoring the gradual transitions at both ends), as depicted in Fig. 40. Previous studies⁴⁹ have derived

formulas for calculating leakage flow by considering leaks as planar areas, but they have neglected the influence of curvature on leakage flow. Taking a circular hole as an example, as shown in Fig. 41, the actual leakage port is formed on the surface of the pipe section, which is a localized cylindrical area and should exhibit a curved surface shape. Previous studies have precisely neglected this aspect. Therefore, focusing on the key aspect of the surface, this article further refines Zheng Chengzhi's approach⁴⁹ to derive an improved leakage flow calculation formula by addressing the surface area and replacing the planar projection area. The specific derivation process is as follows.

A. Round hole

1. Circumferential deformation

According to the principle of stress, the circumferential stress relationship of the pipeline around a round hole is given in Eq. (21). The circumferential deformation is given in Eq. (22).

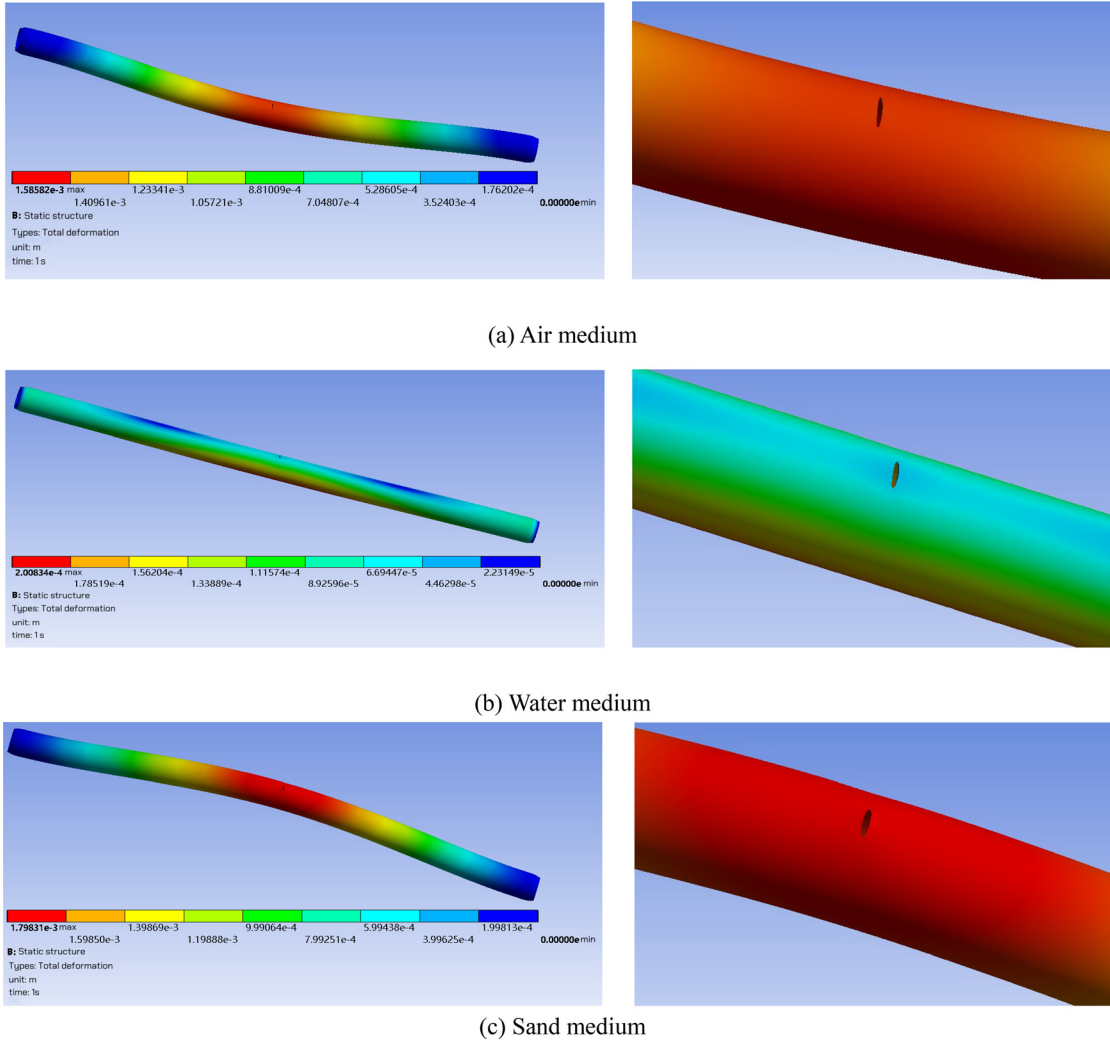


FIG. 32. Deformation cloud diagram of PVC-UH pipeline with circumferential crack.

$$\bar{\sigma}_{cd} = \frac{\Delta d_c}{d_0} E \bar{i}_c, \quad (21)$$

$$d_c = d_0 + \Delta d_c = \left(1 + \frac{\rho g h D_{in}}{2\delta E}\right) d_0 = (1 + C_0 h) d_0. \quad (22)$$

Among them, d_0 is the original leak diameter, measured in m; Δd_c is the circumferential change in leak diameter caused by pressure, measured in m; d_c is the length of the leak diameter in the circumferential direction after being subjected to pressure, measured in m; and C_0 is a constant, with a value of $\frac{\rho g D_{in}}{2\delta E}$.

2. Axial deformation

Using the same method, we obtain Eqs. (23) and (24).

$$\bar{\sigma}_{1d} = \frac{\Delta d_1}{d_0} E \bar{i}_1, \quad (23)$$

$$d_1 = d_0 + \Delta d_1 = \left(1 + \frac{\rho g h D_{in}^2}{4(\delta^2 + D_{in}\delta)E}\right) d_0 = (1 + C_1 h) d_0. \quad (24)$$

Among them, Δd_1 is the axial change in leak diameter caused by pressure, measured in m; and d_1 is the length of the leak diameter in the axial direction after being subjected to pressure, measured in m. C_1 is a constant, with a value of $\frac{\rho g D_{in}^2}{4(\delta^2 + D_{in}\delta)E}$.

3. Radial deformation

Because the radial stress is significantly smaller than the circumferential and axial stresses, and the shape of the leak is circular, it is not prone to outward deformation. Therefore, the influence of radial stress, lateral pressure, and friction on the size of the leak is ignored.

According to Eqs. (22) and (24), determine d_c and d_1 , and solve for the major and minor axes of the elliptical projection of this surface. Since the major axis is along the axial direction, the projection length

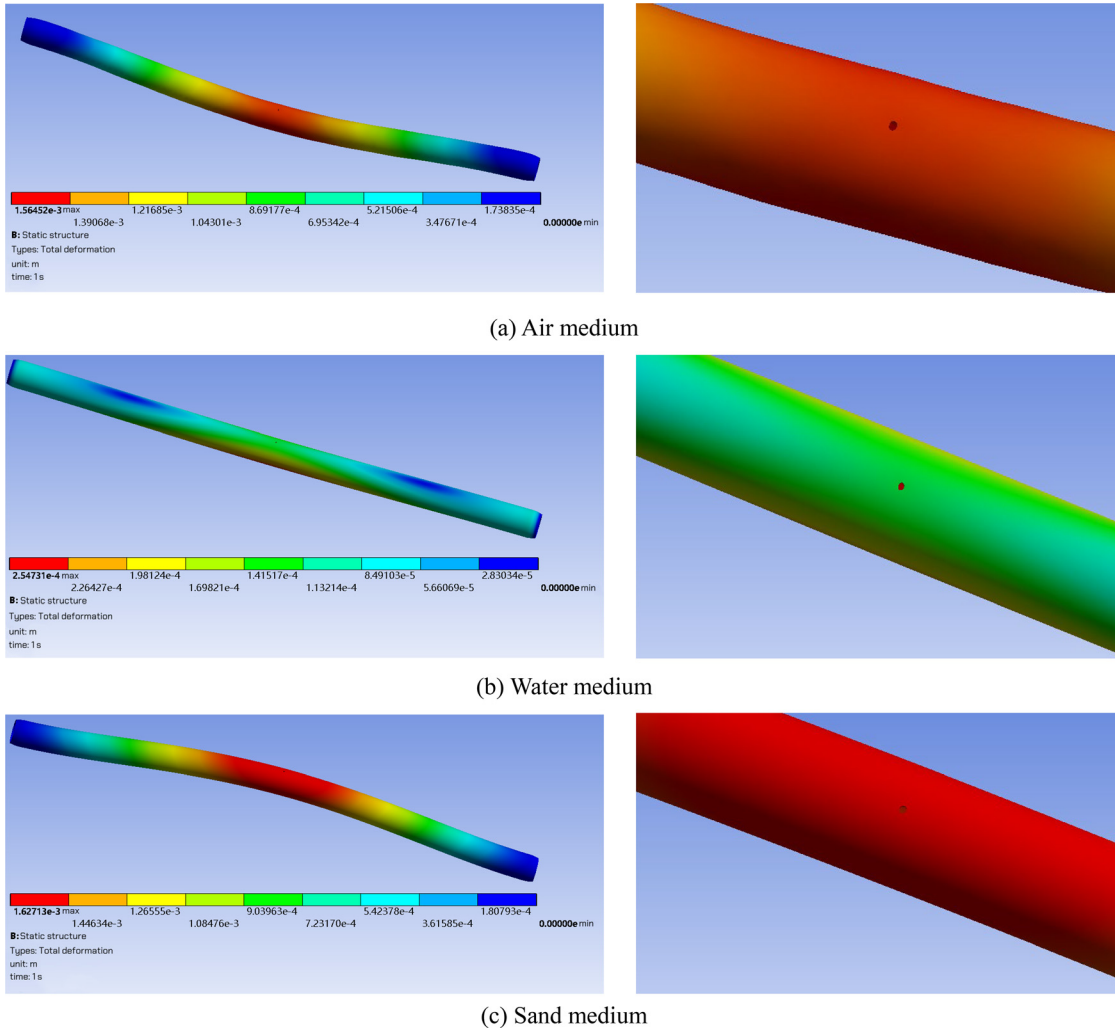


FIG. 33. Deformation cloud diagram of PVC-UH pipeline with round hole.

remains constant, i.e., $d'_1 = d_1$, while the minor axis is circumferential and has a certain degree of curvature, as shown in Fig. 42. $\theta = \frac{d_c}{2R}$ can be obtained from the relationship between arc length and radius. Therefore, the length of the minor axis (chord length) of the elliptical projection surface is $d'_c = 2R \sin \theta = 2R \sin\left(\frac{d_c}{2R}\right)$. The surface area will be determined using surface integration as follows.

Establish a Cartesian coordinate system, as depicted in Fig. 43, with the cylindrical equation given by

$$x^2 + z^2 = R^2. \tag{25}$$

Here, R is the radius of the pipe. According to the above content, it can be seen that the projection surface of the circular leak is an ellipse. Assuming that the elliptical surface is

$$\sum : \frac{x^2}{a^2} + \frac{y^2}{b^2} = 1, \quad d'_1 = 2a, \quad d'_c = 2b. \tag{26}$$

By integrating the curved surface, the formula for calculating the curved surface area is derived and presented in

$$A_r = \iint_{\Sigma} \sqrt{1 + z'^2_x + z'^2_y} dx dy = \iint_{\Sigma} \sqrt{1 + z'^2_x} dx dy. \tag{27}$$

By substituting $z'_x = \frac{-x}{\sqrt{R^2 - x^2}}$ and integrating, the leakage area is determined and presented in

$$A_r = 4bR \cdot \text{EllipticE} \left[\arcsin\left(\frac{a}{R}\right), \frac{R^2}{a^2} \right]. \tag{28}$$

In the formula, $a = \frac{d_1}{2} = \frac{(1+C_1h)d_0}{2}$, $b = \frac{d'_c}{2} = R \sin\left(\frac{d_c}{2R}\right) = R \sin\left(\frac{(1+C_1h)d_0}{2R}\right)$, EllipticE represents the elliptic integral equation. After calculation, the formula for calculating the leakage flow rate of a round hole is

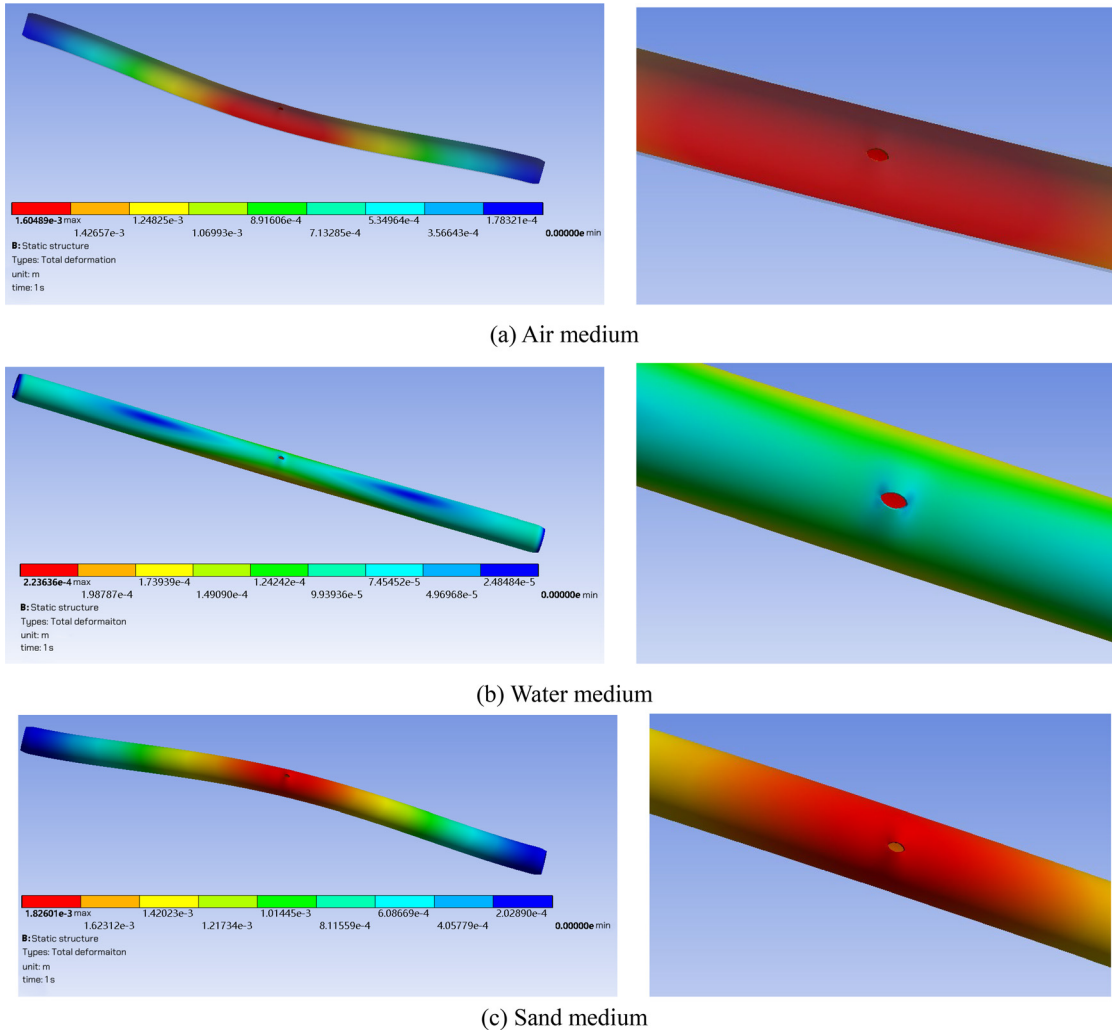


FIG. 34. Deformation cloud diagram of PVC-UH pipeline with axial crack.

$$Q_0 = 4\sqrt{2gh}C_dR^2 \sin \frac{(1 + C_0h)d_0}{2R} \text{EllipticE} \times \left[\arcsin \frac{(1 + C_1h)d_0}{2R}, \frac{4R^2}{(1 + C_1h)^2 d_0^2} \right]. \quad (29)$$

$$\frac{\Delta b_1}{\pi(D_{in} + \delta)} E \bar{i}_c \approx \frac{\Delta b_1}{\pi(D_{in} + \delta) + \Delta b_1} E \bar{i}_c = \bar{\sigma}_{cd}. \quad (30)$$

In the equation, Δb_1 is the change in width of the central part of the axial crack, measured in m, and Eq. (31) is derived from Eqs. (30) and (21).

$$\Delta b_1 = \frac{\pi \rho g (D_{in}^2 + D_{in} \delta)}{2E\delta} h = C_2 h. \quad (31)$$

C_2 is a constant with a value of $\frac{\pi \rho g (D_{in}^2 + D_{in} \delta)}{2E\delta}$. The width of the central part of the axial crack under pressure is given by

$$b_1 = b_0 + \Delta b_1 = b_0 + C_2 h. \quad (32)$$

2. Axial deformation

Neglecting the variation in axial crack length, no stress analysis will be conducted on this type of crack in the axial direction.

B. Axial crack

1. Circumferential deformation

When the length of the axial crack is zero, the change in circumferential stress at the edge of the crack is zero. When the length of the axial crack reaches a certain value, this value is defined as the critical length for circumferential force. When the length of the axial crack exceeds or equals critical length for circumferential force, the change in circumferential stress at the center edge of the crack is the stress experienced prior to failure. The change in width of the crack center can be obtained as shown in

09 January 2025 04:38:34

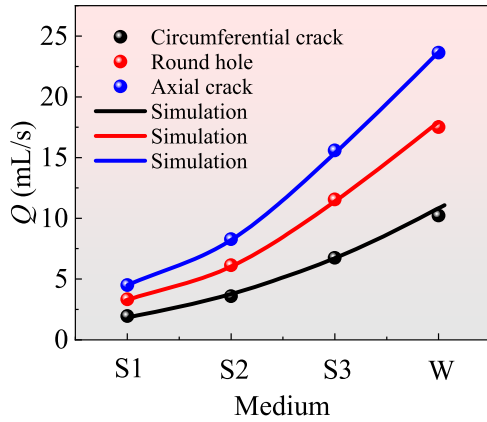


FIG. 35. Comparison between finite element analysis and experiment results.

3. Other deformations

Axial cracks can cause the edges of the crack to turn outward and expand the leakage area under the action of radial stress, lateral pressure, and friction. Assuming that these stresses cause the crack width to change linearly with the water head, the following equation is derived:

$$b'_1 = b_1(1 + kh) = (b_0 + C_2h)(1 + kh) = b_0 + C_2h + b_0kh + C_2kh^2. \tag{33}$$

TABLE XII. Parameter values. Note: l is the length of the circumferential and axial cracks, and the diameter of the round holes in parentheses.

Parameters	Unit	Values
$l(d)$	mm	10(3.6), 20(5.0), 30(6.2), 40(7.1), 50(8.0), 60(8.7), 70(9.4)
D	mm	25, 50, 70, 90, 110, 130, 150, 200
t	mm	3, 4, 6, 8, 10, 12, 14
E	MPa	1500, 2000, 3500, 5000, 8000, 12000

The ellipse formed by this surface on the projection plane has its major and minor axes of $l_0 = 2a$ and $b''_1 = 2R \sin \theta = 2R \sin\left(\frac{b'_1}{2R}\right) = 2b$, respectively. Therefore, the following equation can be obtained:

$$a = \frac{l_0}{2}, \quad b = R \sin\left(\frac{b_0 + C_2h + b_0kh + C_2kh^2}{2R}\right). \tag{34}$$

Substituting a and b into Eq. (27) yields

$$A_r = 4R^2 \sin\left(\frac{b_0 + C_2h + b_0kh + C_2kh^2}{2R}\right) \text{EllipticE}\left(\arcsin\frac{l_0}{2R}, \frac{4R^2}{l_0^2}\right). \tag{35}$$

After calculation, the formula for calculating the axial crack leakage flow rate is presented in

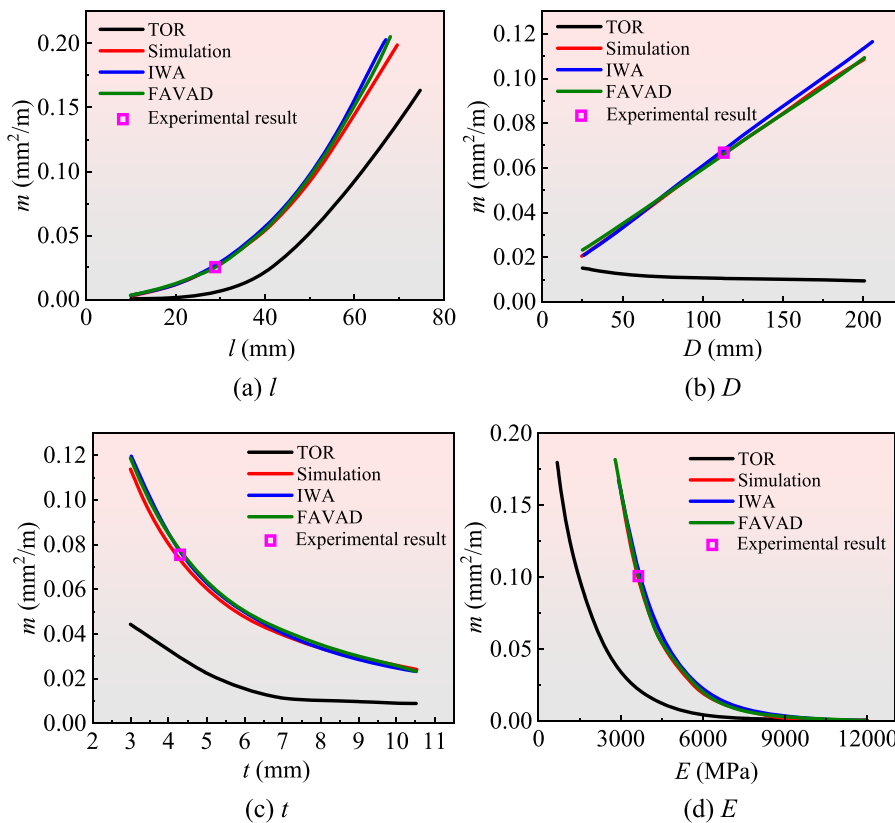


FIG. 36. Comparison of finite element results of circumferential cracks with existing models.

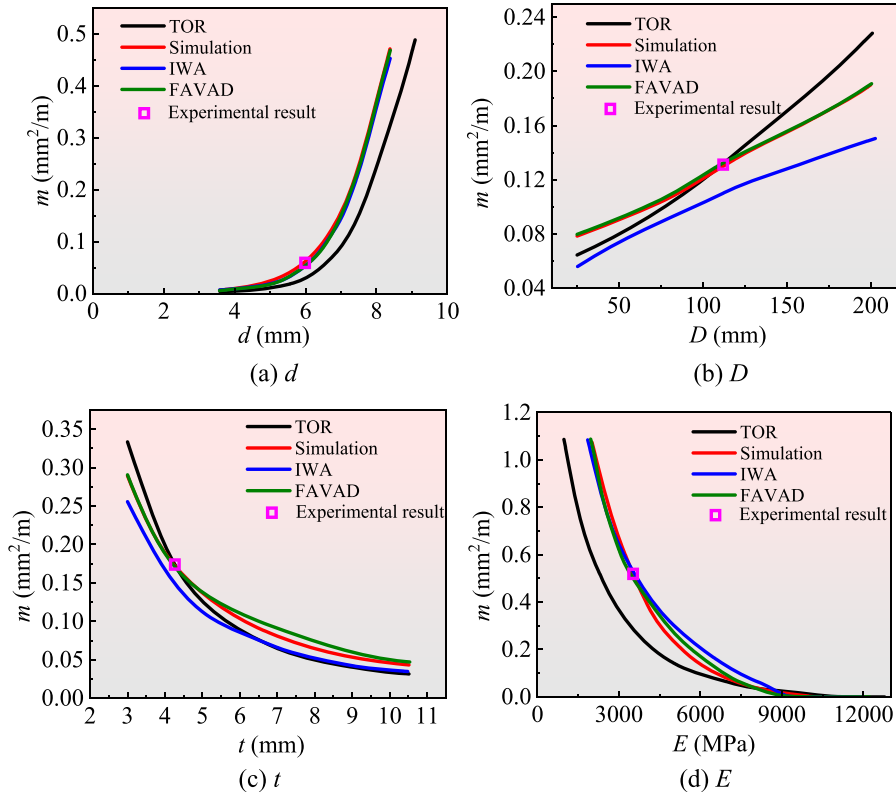


FIG. 37. Comparison of finite element results of round holes with existing models.

09 January 2025 04:38:34

$$Q_l = 4\sqrt{2gh}C_dR^2 \sin\left(\frac{b_0 + C_2h + b_0kh + C_2kh^2}{2R}\right) \text{EllipticE} \times \left(\arcsin \frac{l_0}{2R}, \frac{4R^2}{l_0^2}\right). \tag{36}$$

C. Circumferential crack

The experimental section is connected to the system via the Haval joint. Due to the circumferential crack, the pipeline is fixed at both ends, and the axial force (tensile stress) is constrained during elongation of the pipeline. The elongation at both ends will reduce the width of the existing crack, and the corresponding relationship is given in

$$\frac{-\Delta b'_2}{L_{\text{fix}}} E \bar{i}_1 = \bar{\sigma}_{1d}. \tag{37}$$

In the equation, $\Delta b'_2$ is the change in width of the central part of the circumferential crack, and L_{fix} is the distance between the fixed points at both ends of the pipeline where the circumferential crack is located, measured in m. By combining Eq. (23), the decrease in width of the central part of the circumferential crack is obtained and presented in

$$\Delta b'_2 \bar{i}_1 = -L_{\text{fix}} \frac{\bar{\sigma}_{1d}}{E} = -C_5 h \bar{i}_1. \tag{38}$$

In the equation, $C_5 = \frac{L_{\text{fix}} \rho g D_m^2}{4(\delta^2 + D_m \delta) E}$. At this point, the width of the circumferential crack is given by

$$b = b_0 - C_5 h. \tag{39}$$

Assuming the initial circumferential crack arc length is l_1 , due to the b equivalence transformation, the projection surface is rectangular, thus eliminating the need for surface integration. The surface area of the circumferential crack is directly obtained and presented in

$$A_r = (b_0 - C_5 h) l_1. \tag{40}$$

The calculation formula for the circumferential crack leakage flow rate can be obtained by substituting Eq. (40) into Eq. (14), which is

$$Q_c = \sqrt{2gh} C_d (b_0 - C_5 h) l_1. \tag{41}$$

It should be noted that Eqs. (29), (36), and (41) present the calculation formulas for the leakage flow rates of three types of free outflow forms (air medium). For submerged outflow and sand outflow, there are no relevant formulas to refer from in previous studies. When referring to submerged outflow at the orifice, the principle of effective head is considered, which is assumed to be h_0 .⁶⁵ Therefore, to obtain the flow rate formulas for each medium outflow, it is assumed that h in each formula is represented as the effective head h_0 . As shown in Eqs. (42)–(44).

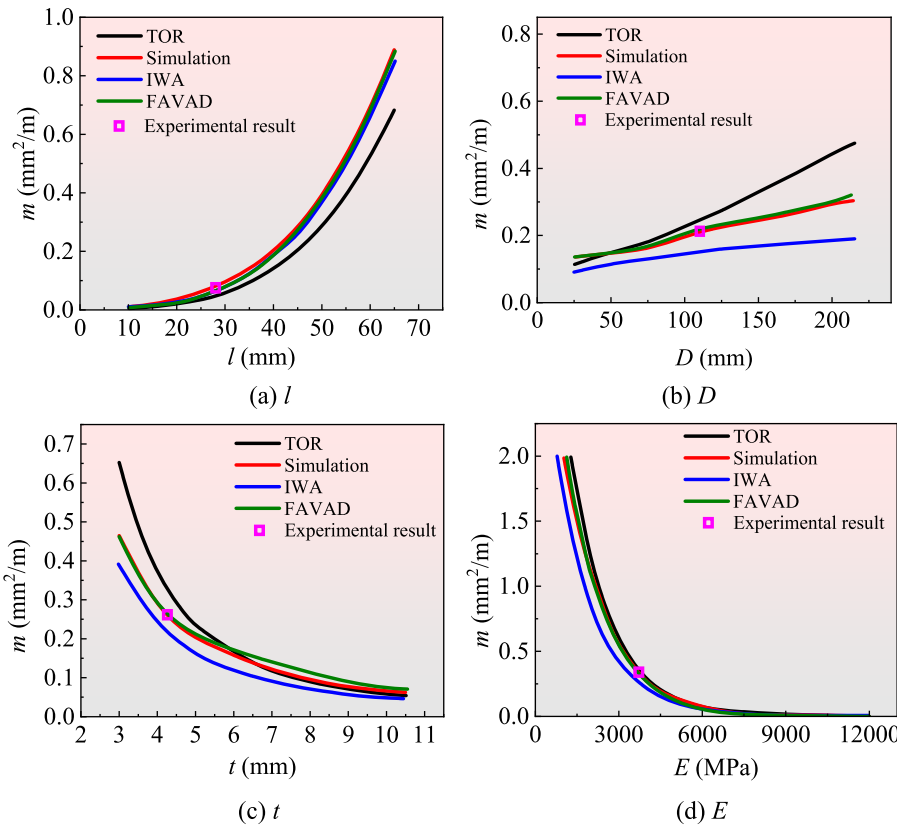


FIG. 38. Comparison of finite element results of axial cracks with existing models.

(1) The improved round hole FAVAD model is given by

$$Q_0 = 4\sqrt{2gh_0}C_dR^2 \sin\left(\frac{1+C_0h_0}{2R}d_0\right) \text{EllipticE} \times \left[\arcsin\left(\frac{1+C_1h_0}{2R}d_0\right), \frac{4R^2}{(1+C_1h_0)^2d_0^2} \right]. \quad (42)$$

(2) The improved axial crack FAVAD model is given by

$$Q_1 = 4\sqrt{2gh_0}C_dR^2 \sin\left(\frac{b_0+C_2h_0+b_0kh_0+C_2kh_0^2}{2R}\right) \text{EllipticE} \times \left(\arcsin\left(\frac{l_0}{2R}, \frac{4R^2}{l_0^2}\right) \right). \quad (43)$$

(3) The improved circumferential crack FAVAD model is given by

$$Q_c = \sqrt{2gh}C_d(b_0 - C_5h_0)l_1. \quad (44)$$

When the medium is water, h_0 is given by

$$h_0 = h - h_w. \quad (45)$$

When the medium is sand, the equivalent water depth h_w can be used to express it. As shown in

$$\rho_w g h_w = \rho_s g h_s, \quad (46)$$

$$h_w = \frac{\rho_s h_s}{\rho_w}, \quad (47)$$

h_w is the depth of water in the iron box, h_s is the burial depth of saturated sand in the iron box. Therefore, the effective water head when the medium is sand is given by

$$h_0 = h - \frac{\rho_s h_s}{\rho_w}. \quad (48)$$

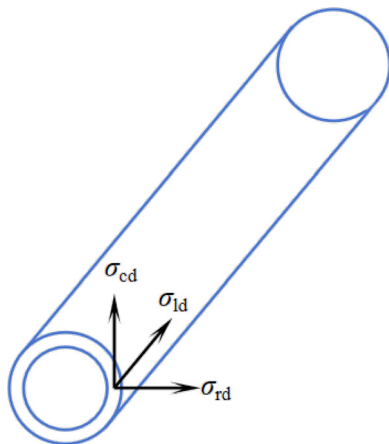


FIG. 39. Pressure bearing pipeline stress.

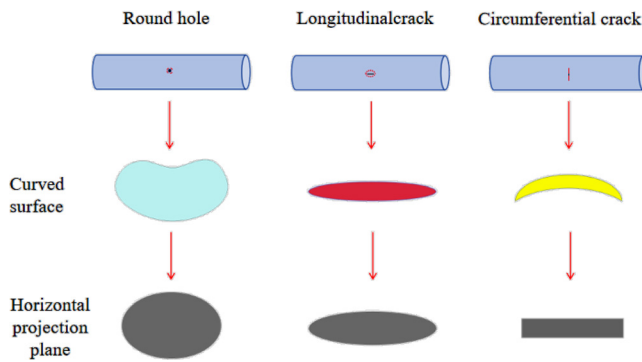


FIG. 40. Projection surface of leakage considering curvature.

Applying Eqs. (42)–(44) to the calculation of leakage flow rates, and combining them with existing relevant computational models—namely those of Latifi *et al.*,⁴¹ Shi,⁶⁶ Shahangian *et al.*,⁶⁵ and Sam *et al.*⁴ (only axial cracks)—we compare these with experimental results as depicted in Fig. 44. The figure shows that the calculated results of the improved FAVAD model and the S.S.A model are consistent with the test values, indicating that these models can be used to calculate the leakage flow. However, both the M. Latifi and F. Sam models overestimated the test values, possibly because the M. Latifi model, fitted by its own test results, exhibits certain deviations when applied to this study. The axial crack calculated by the F. Sam model is on the side of the pipe, leading to a certain impact due to gravity. However, in this study, the crack is at the top of the pipe, and the effect of gravity is neglected. The T. Shi model underestimated the test value in this study and calculated conservatively, possibly because it ignored the actual curved surface deformation of the leakage and treated it as a planar projection.

Considering the limited factors considered in this study, the test results exhibit certain limitations. In the future, the influence of sand grading characteristics (both continuous and discontinuous), various leakage mouth shapes (e.g., triangular and square), the viscoelastic properties of the pipeline, and external traffic loads on leakage characteristics can be further investigated through additional testing to obtain more data. To better understand the leakage mechanism.

VI. CONCLUSIONS

This study designs three types of leaks, namely circumferential cracks, circular holes, and axial cracks. Leakage simulation tests were

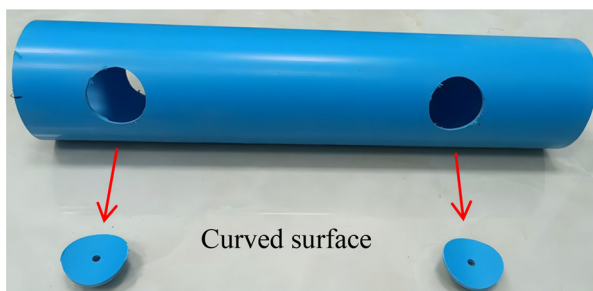


FIG. 41. Curved surface.

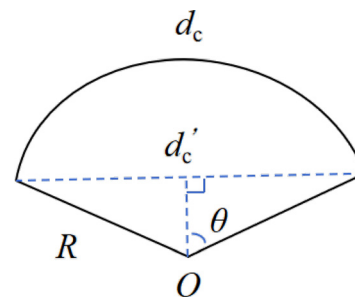


FIG. 42. Chord length diagram.

conducted on 39 pipe sections, considering factors such as the surrounding medium (air, water, and sand) and burial depths (200, 400, and 600 mm). The study aims to obtain the relationship between leakage flow rate and pressure, analyze the experimental results using existing theoretical models, quantitatively analyze the changing trends of leakage evaluation indicators (m , C_d) based on the FAVAD model, and then perform finite element verification to obtain the velocity distribution within the flow field and the deformation characteristics of the pipeline. Further parameter expansion analysis is conducted to determine the influence of leakage size (l , d), pipeline outer diameter (D), wall thickness (t), and elastic modulus (E) on the value of m . Finally, considering the influence of leakage curvature, the derivation and improvement of the leakage flow calculation formula were performed based on the FAVAD model. The main conclusions drawn from this study are as follows.

- (1) In sand media, an “inverted cone” sand-water mixing zone is formed below, and a “semi-elliptical” erosion pit with cracks is formed above. In water media, a “seismic source” forms on the surface of the water body directly above the leakage port, propagating in the form of water waves to the surrounding area. In the air medium, when the water pressure is low, only a water column is sprayed in the middle of the axial crack. As the water pressure increases, the water column widens along the length of the crack and thickens along its width. The width of the water column in the middle is slightly larger. Applying small water pressure to circumferential cracks and circular leaks can cause water jets to spray throughout the entire length of the crack.
- (2) The leakage flow rate Q increases with the increase in pressure h . When all other conditions are the same, the order of the leakage flow rate Q is free outflow > submerged outflow > sand outflow, and the increase increases in Q with increasing pressure. When considering the influence of surrounding media, the IWA and FAVAD models can be used to approximate the leakage flow rate. The change in the leakage flow rate shows an increasing trend, on average, in the order of circumferential cracks, circular holes, and axial cracks. Among them, the variation amplitude of circumferential cracks is relatively small, while the average leakage flow rate of circular holes and axial cracks shows a clear increasing trend.
- (3) When other conditions are the same, the leakage flow rate increases in the order of S1, S2, S3, W, and A with changes in the medium and decreases with increases in burial depth H . The slope is smaller when transitioning from S1 to S2, and then the slope of the curve becomes larger. The descent speed of Q is greater when H increases from 200 to 400 mm than when H

09 January 2025 04:38:34

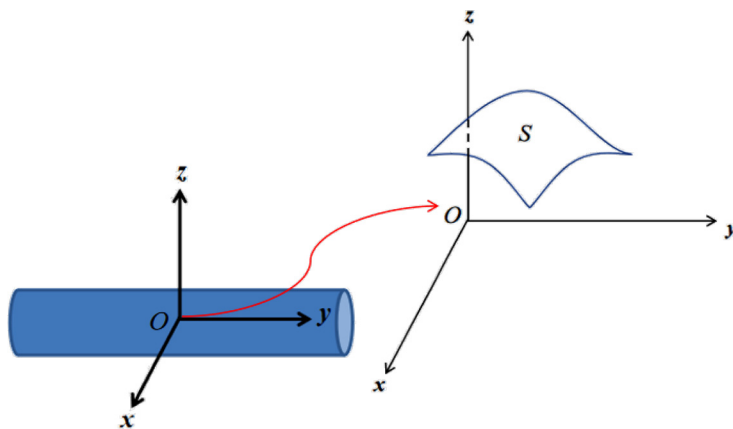


FIG. 43. Cartesian coordinate system.

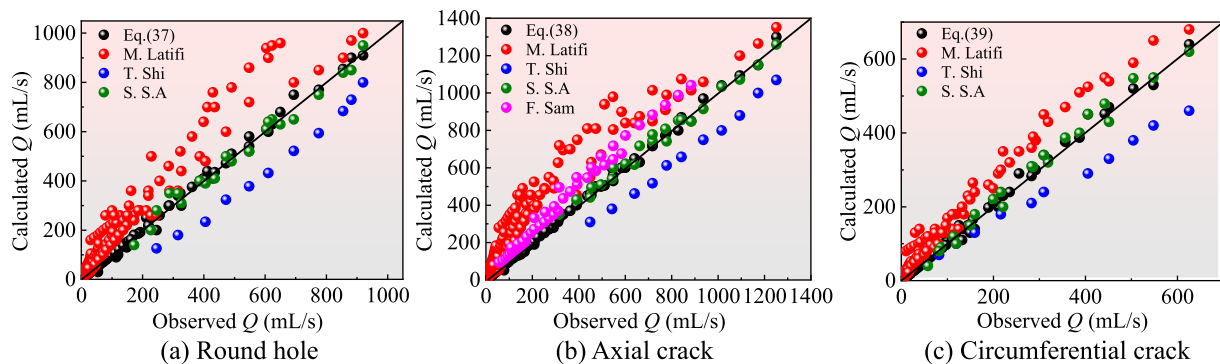


FIG. 44. Comparison of models and experimental results.

increases from 400 to 600 mm. The greater the applied pressure, the more significant the amplitude of the above changes.

- (4) The m value increases with the increase in k and decreases with the increase in $\gamma_d H$. The slope of the m value change for different types of leaks at different burial depths is roughly equal, but the m value in S1 and S2 media is smaller than that in S3. C_d increases with the increase in k , and the changes are roughly similar. When the burial depth is 600 mm, the increase in C_d is relatively small. C_d decreases with the increase in $\gamma_d H$, and the variation pattern across different burial depths is roughly the same. The absolute value of the slope for the circumferential crack (corresponding to S3) is larger than those of the circular and axial cracks.
- (5) The fluid flow velocity at the leakage port is significantly higher than that in a normal pipeline, with the maximum flow velocity occurring at the center of the port. The velocity distribution of the leaked fluid at each leak is approximately in the shape of an inverted cone, with a relatively high velocity of around 25 m/s in the air medium and a relatively low velocity of around 5 m/s in the sand medium. The final deformation of each leak is approximately elliptical, with the order of deformation being circumferential crack < circular leak < axial crack.
- (6) Except for the TOR model, the m values of all models for circumferential cracks increase approximately linearly with the increase in D , increase approximately exponentially with the increase of $l(d)$, and decrease approximately exponentially

with t and E . For circular leaks and axial cracks, neither the TOR model nor the IWA model matches well with the finite element method. Only the FAVAD model is consistent with both the finite element method and the experimental results. The improved FAVAD model [Eqs. (42)–(44)] and S.S.A model provide ideal and reliable results, which can be applied to the calculation of the leakage flow rate for buried pipelines.

ACKNOWLEDGMENTS

This research work was financially supported by the National Key Research and Development Program of China (Grant No. 2022YFC3004401), the Program of Taishan Industry Leading Talent Project (Grant No. tscx202306104), the National Natural Science Foundation of China (Grant No. 52130901), and the Natural Science Foundation of Henan (Grant No. 232300421003).

AUTHOR DECLARATIONS

Conflict of Interest

The authors have no conflicts to disclose.

Author Contributions

Zongyuan He: Data curation (equal); Formal analysis (equal); Investigation (equal); Methodology (equal); Visualization (equal); Writing – original draft (equal). **Shaowei Hu:** Funding acquisition

09 January 2025 04:38:34

(lead); Project administration (lead); Writing – review & editing (lead). **Changxi Shan:** Supervision (equal); Writing – review & editing (equal). **Fuqu Pan:** Supervision (equal); Writing – review & editing (equal).

DATA AVAILABILITY

The data that support the findings of this study are available within the article.

REFERENCES

- ¹D. Zhao, “Research on tube burst monitoring method based on SCADA system,” M.A. thesis, (Zhejiang University, Hangzhou, China, 2014) (in Chinese).
- ²F. Maietta, G. Crispino, C. Capponi *et al.*, “Transient response of hybrid and homogeneous pipelines: Laboratory experiments,” *Phys. Fluids* **36**(3), 035113 (2024).
- ³A. He, “Study on assessment and identification of major hazard sources in subway construction,” M.A. thesis, Zhongnan University, Changsha, China, 2010 (in Chinese).
- ⁴F. Sam, R. Collins, and J. Boxall, “Physical investigation into the significance of ground conditions on dynamic leakage behaviour,” *J. Water Supply: Res. Technol.—AQUA* **65**(2), 103–115 (2016).
- ⁵Z. Van and R. Malde, “Evaluating the pressure-leakage behaviour of leaks in water pipes,” *J. Water Supply: Res. Technol.—AQUA* **66**(5), 287–299 (2017).
- ⁶V. Streeter, E. Wylie, and K. Bedford, *Fluid Mechanics*, 9th ed. (WCB/McGraw Hill, Boston, MA, USA, 1998).
- ⁷F. Marco and L. Lanza, “Leaks in pipes: Generalizing Torricelli’s equation to deal with different elastic materials, diameters and orifice shape and dimensions,” *Urban Water J.* **11**(8), 678–695 (2014).
- ⁸M. Farley and S. Trow, *Losses in Water Distribution Networks: A Practitioner’s Guide to Assessment, Monitoring and Control* (IWA Publishing, 2005).
- ⁹T. Walski, W. Bezts, E. Posluszny *et al.*, “Modeling leakage reduction through pressure control,” *J. Am. Water Works Assoc.* **98**(4), 147–155 (2006).
- ¹⁰J. Thronton, “Managing leakage by managing pressure: A practical approach,” *Water* **21** 6(1), 43–44 (2003).
- ¹¹J. May, “Pressure dependent leakage,” World Water and Environmental Engineering, Water Environment Federation, Washington, DC, USA, 1994.
- ¹²A. Ashcroft and D. Taylor, “Ups and downs of flow and pressure,” *Surveyor* **162**, 16–18 (1983).
- ¹³U. Sendil and K. Dhowalia, “Relationship between pressure and leakage in a water distribution network,” in Proceedings of the AWWA Conference, 1992.
- ¹⁴L. Allan, “What do we know about pressure-leakage relationships in distribution systems,” in Proceedings of the IWA Conference on Systems Approach to Leakage Control and Water Distribution System Management, 2001.
- ¹⁵J. Thornton and L. Allan, “Progress in practical prediction of pressure: Leakage, pressure: Burst frequency and pressure: Consumption relationships,” in Proceedings of IWA Special Conference ‘Leakage, 2005.
- ¹⁶M. Khadam, N. Shammam, and Y. Al-Feraiheedi, “Water losses from municipal utilities and their impacts,” *Water Int.* **16**(4), 254–261 (1991).
- ¹⁷A. Cassa, Z. Van, and R. F. Laubscher, “A numerical investigation into the effect of pressure on holes and cracks in water supply pipes,” *Urban Water J.* **7**(2), 109–120 (2010).
- ¹⁸Y. Li *et al.*, “Estimation of leak area-pressure relationship for cracks on water pipes using models based on linear-elastic fracture mechanics,” *Water Res.* **221**, 118692 (2022).
- ¹⁹Y. Wu, X. Ou, B. Wu *et al.*, “Numerical simulation of water and sediment flow characteristics in tunnels based on Euler–Euler three-phase flow,” *Phys. Fluids* **36**(2), 023354 (2024).
- ²⁰C. Xie, Z. Pan, Z. Wu *et al.*, “Mechanical behavior of water ingress process for the locally damaged submerged floating tunnel and its interpretation: A full-length experimental study,” *Phys. Fluids* **36**(10), 107125 (2024).
- ²¹K. He, H. Shi, and X. Yu, “Effects of interstitial water on collapses of partially immersed granular columns,” *Phys. Fluids* **34**(2), 023306 (2022).
- ²²W. Meng, L. Liao, C. Yu *et al.*, “Eulerian–Eulerian multiphase models for simulating collapse of submarine sediment column with rheological characteristics in air–water flow,” *Phys. Fluids* **33**(11), 113301 (2021).
- ²³C. Guo, Y. Li, X. Nian *et al.*, “Experimental study on the slip velocity of turbulent flow over and within porous media,” *Phys. Fluids* **32**(1), 015111 (2020).
- ²⁴X. Qi, S. Liu, Z. Yu *et al.*, “Interfacial dynamics of gas–water displacement in fractured porous media under high pressure,” *Phys. Fluids* **33**(9), 092003 (2021).
- ²⁵K. Zhao, L. Qiu, and Y. Liu, “Two-layer two-phase material point method simulation of granular landslides and generated tsunami waves,” *Phys. Fluids* **34**(12), 123312 (2022).
- ²⁶X. Luo, T. Chen, W. Xiao *et al.*, “The dynamics of a bubble in the internal fluid flow of a pipeline,” *Phys. Fluids* **34**(11), 117103 (2022).
- ²⁷H. Hattori, A. Wada, M. Yamamoto *et al.*, “Experimental study of laminar–turbulent transition in pipe flow,” *Phys. Fluids* **34**(3), 034115 (2022).
- ²⁸V. Tjuatja, A. Keramat, B. Pan *et al.*, “Transient flow modeling in viscoelastic pipes: A comprehensive review of literature and analysis,” *Phys. Fluids* **35**(8), 081302 (2023).
- ²⁹G. Germanopoulos and P. Jowitt, “Leakage reduction by excess pressure minimization in a water supply network,” *Proc. Inst. Civ. Eng.* **87**(2), 195–214 (1989).
- ³⁰B. Rajani and C. Zhan, “On the estimation of frost loads,” *Can. Geotech. J.* **33**(4), 629–641 (1996).
- ³¹Y. Kleiner and B. Rajani, “Comprehensive review of structural deterioration of water mains: Statistical models,” *Urban Water* **3**(3), 131–150 (2001).
- ³²M. Seica, J. Packer, M. W. F. Grabinsky *et al.*, “Evaluation of the properties of toronto iron water mains and surrounding sand,” *Can. J. Civ. Eng.* **29**(2), 222–237 (2002).
- ³³H. Najjaran, R. Sadiq, and B. Rajani, “Fuzzy expert system to assess corrosion of cast/ductile iron pipes from backfill properties,” *Comput.-Aided. Civ. Infrastruct. Eng.* **21**(1), 67–77 (2006).
- ³⁴Q. Xu, R. Liu, Q. Chen *et al.*, “Review on water leakage control in distribution networks and the associated environmental benefits,” *J. Environ. Sci.* **26**(5), 955–961 (2014).
- ³⁵T. Walski, W. Bezts, E. Posluszny *et al.*, “Understanding the hydraulics of water distribution system leaks,” in *Critical Transitions in Water and Environmental Resources Management* (American Society of Civil Engineers, 2004), pp. 4799–4808.
- ³⁶C. Noack and B. Ulanicki, “Modelling of sand diffusibility on leakage characteristics of buried pipes,” in Proceedings of the Water Distribution Systems Analysis Symposium, 2008.
- ³⁷Z. Van and C. Clayton, “The effect of pressure on leakage in water distribution systems,” *Proc. Inst. Civil Eng.—Water Manage.* **160**(2), 109–114 (2007).
- ³⁸Z. Van, “Theoretical modeling of pressure and leakage in water distribution systems,” *Procedia Eng.* **89**, 273–277 (2014).
- ³⁹Z. Van, M. Alsaydalani, C. Clayton *et al.*, “Soil fluidisation outside leaks in water distribution pipes—Preliminary observations,” *Proc. Inst. Civil Eng. - Water Manage.* **166**(10), 546–555 (2013).
- ⁴⁰S. Pike, Z. Van, and C. Clayton, “Scouring damage to buried pipes caused by leakage jets: Experimental study,” *J. Pipeline Syst. Eng. Pract.* **9**(4), 04018020 (2018).
- ⁴¹M. Latifi, S. Naeeni, and A. Mahdavi, “Experimental assessment of sand effects on the leakage discharge from polyethylene pipes,” *Water Sci. Technol. Water Supply* **18**(2), 539–554 (2018).
- ⁴²M. Latifi, R. Parvaneh, and S. Naeeni, “Investigating the influence of surrounding sand properties on leakage discharge from cracks in polyethylene pipes,” *Eng. Fail. Anal.* **141**, 106676 (2022).
- ⁴³M. Latifi, S. Mohammadbeigi, M. Farahi *et al.*, “Experimental study of pressure and soil effects on fluidization and mobile bed zones around buried leaking pipes,” *J. Pipeline Syst. Eng. Pract.* **13**(4), 04022034 (2022).
- ⁴⁴CJT493-2016, “High performance unplasticized poly (vinyl chloride) pipes and fittings for water supply,” Standard No. CJT493-2016. (Standards Press of China, Beijing, 2016) (in Chinese).
- ⁴⁵International Standard, “Thermoplastic pipes—determination of tensile properties—Part 2: Pipes made of unplasticized poly (vinyl chloride) (PVC-U), chlorinated poly (vinyl chloride) (PVC-C) and high-impact poly (vinyl chloride) (PVC-HI),” (China Standards Press, Beijing, 2003) (in Chinese).
- ⁴⁶CJJ 101-2016, “Technical specification for buried plastic pipeline of water supply engineering,” Standard No. CJJ 101-2016 (China Building Industry Press, Beijing, 2016) (in Chinese).

- ⁴⁷GB 50021–2001, “Code for investigation of geotechnical engineering,” Standard No. GB 50021–2001 (China Building Industry Press, Beijing, 2009) (in Chinese).
- ⁴⁸GB/T 50123–2019, “Standard for sand test method,” Standard No. GB/T 50123–2019 (China Planning Press, Beijing, 2019) (in Chinese).
- ⁴⁹C. Zheng, “Research on physical leakage flow analysis model of water supply network based on signal processing algorithm,” Ph.D. thesis, Harbin Institute of Technology, Harbin, China, 2015 (in Chinese).
- ⁵⁰A. Cassa, “A numerical investigation into the behaviour of cracks in UPVC pipes under pressure,” Ph.D. thesis, University of Johannesburg, South Africa, 2011.
- ⁵¹P. Jowitt and C. Xu, “Optimal valve control in water-distribution networks,” *J. Water Resour. Plann. Manage.* **116**(4), 455–472 (1990).
- ⁵²L. Araujo, S. S. H. Coelho, and C. Ramos, “Estimation of distributed pressure-dependent leakage and consumer demand in water supply networks,” in *Advances in Water Supply Managment*, edited by C. Maksimovic, D. Butler, F. A. Memon (Swets and Zeitlinger, Lisse, 2003), pp. 119–128.
- ⁵³J. Parker and E. Park, “Modeling field-scale dense nonaqueous phase liquid dissolution kinetics in heterogeneous aquifers,” *Water Resour. Res.* **40**(40), 191–201, <https://doi.org/10.1029/2003wr002807> (2004).
- ⁵⁴B. Kueper and E. Frind, “Two-phase flow in heterogeneous porous media: 2. Model application,” *Water Resour. Res.* **27**(6), 1059–1070, <https://doi.org/10.1029/91WR00267> (1991).
- ⁵⁵W. Zhong, Y. Xiong, Z. Yuan *et al.*, “DEM simulation of gas-solid flow behaviors in spout-fluid bed,” *Chem. Eng. Sci.* **61**(5), 1571–1584 (2006).
- ⁵⁶X. Zhao, S. Li, G. Liu *et al.*, “DEM simulation of the particle dynamics in two-dimensional spouted beds,” *Powder Technol.* **184**(2), 205–213 (2008).
- ⁵⁷Z. Yong, B. Jin, W. Zhong *et al.*, “DEM simulation of particle mixing in flat-bottom spout-fluid bed,” *Chem. Eng. Res. Des.* **88**(5–6), 757–771 (2010).
- ⁵⁸R. Bing, W. Zhong, B. Jin *et al.*, “Computational fluid dynamics (CFD)-discrete element method (DEM) simulation of gas-solid turbulent flow in a cylindrical spouted bed with a conical base,” *Energy Fuels* **25**, 4095–4105 (2011).
- ⁵⁹S. Wang, “Numerical simulation techniques of solid particle erosion and their examination in submarine pipelines,” M.A. thesis (Tianjin University, Tianjin, China, 2013) (in Chinese).
- ⁶⁰P. Roache, “Quantification of uncertainty in computational fluid dynamics,” *Annu. Rev. Fluid Mech.* **29**(1), 123–160 (1997).
- ⁶¹C. Freitas, “The issue of numerical uncertainty,” *Appl. Math. Modell.* **26**(2), 237–248 (2002).
- ⁶²P. Roache, “Error bars for CFD,” in *Proceedings of the 41st Aerospace Sciences Meeting and Exhibit* (AIAA, 2003).
- ⁶³P. Manna, M. Dharavath, P. K. Sinha *et al.*, “Optimization of a flight-worthy scramjet combustor through CFD,” *Aerosp. Sci. Technol.* **27**, 138–146 (2013).
- ⁶⁴A. Zahoor, *Ductile Fracture Handbook*, EPRI NP-6301-D N14-1, Research Project 1757–69, U.S. Electric Power Research Institute, 1989.
- ⁶⁵S. Shahangian, M. Tabesh, and M. Mirabi, “Effects of flow hydraulics, pipe structure and submerged jet on leak behaviour,” *Civil Eng. Infrastruct. J.* **52**(2), 225–243 (2019).
- ⁶⁶T. Shi, “Research on accurate simulation of leakage of pipe network by improved FAVAD model,” M.A. thesis (Harbin Institute of Technology, Harbin, China, 2018) (in Chinese).